APPLICATION OF COMPUTATIONAL FLUID DYNAMICS (CFD) TO STUDY LIQUEFIED NATURAL GAS (LNG) POOL FIRES

A Thesis

by

DUSHYANT MADHAV CHAUDHARI

Submitted to the Office of Graduate and Professional Studies of
Texas A&M University
in partial fulfillment of the requirements for the degree of

MASTER OF SCIENCE

Chair of Committee,	M. Sam Mannan
Committee Members,	Charles Glover
	Rashid Hasan
Head of Department,	Nazmul Karim

December 2016

Major Subject: Chemical Engineering

ABSTRACT

Liquefied Natural Gas (LNG) pool fires pose a major risk to LNG facilities. The radiant energy from a LNG pool fire can be sufficiently high to threaten the structural integrity of the facility, plant personnel, fire fighters and potentially people beyond the boundaries of the facility. Safety analysis for LNG consequence modeling requires protection of the public against hazards caused by LNG pool fires. Current safety analysis involves the use of empirical models to assess the effects of a pool fire. Application of these models to pool fires of different size pose significant uncertainty in terms of underestimation of key parameters.

In this study, a CFD (Computational Fluid Dynamic) software is used to advance the knowledge of LNG pool fire modeling. The Fire Dynamic Simulator (FDS) code is used to simulate pool fire of a small scale experiment to study the sensitivity of different pool fire characteristics on turbulence models.

Comparative study of Deardorff turbulence model and constant coefficient Smagorinsky turbulence model was done to see its dependence on combustion model which eventually affects the radiation. Numerical approach used for determining flame geometry was validated by comparing the results with the experiment. Transient fluctuations of the fire were studied to understand the accuracy of fire dynamics captured by FDS. A visual estimation of extents of a three zone representation of pool fire structure was done by observing temperature and vertical velocity profile.

This work provides information on sensitivity of pool fire on turbulence model and showed that the use of Deardorff turbulence model gave predictions of radiation, flame length and height closer to experimental values than the constant coefficient Smagorinsky turbulence model. Iso-surface of 450℃ was found to describe the flame geometry of the experiment considered. Pulsation frequency obtained from FDS was compared with experimental data and thus shows the accuracy of FDS in capturing transient fluctuations of fire.

ACKNOWLEDGEMENTS

I would like to first acknowledge my adviser and committee chair, Dr. M Sam Mannan, for giving me this opportunity to perform this research by accepting me into Mary Kay O'Conner Process Safety Center. I feel great pride to be part of this group which has helped me learn a lot throughout my graduate studies. I also thank him for showing me correct direction in a subtle way when I struggled with myriad of problems.

I also want to thank my committee members, Dr. Charles Glover and Dr. Rashid Hasan for their time and advice for successful completion of this research.

I take this opportunity to thank Dr. Ray Mentzer and Dr. Nirupama Gopalaswami for supporting me to continue this work with their guidance and advice. I am grateful to Dr. Delphine Laboureur and Monir Ahammad for spending time out of their busy schedule to give me support and technical guidance when most needed.

Thanks also to my friends and colleagues for believing in me and motivating me to proceed with this research. This work could not have been possible without the moral support from all of them. This great experience was more fun because of them.

Finally, thanks to my lovely family back home in India for their patience of understanding my involvement in graduate studies and encouragement at every step of this endeavor.

NOMENCLATURE

LNG	Liquefied Natural Gas
RPT	Rapid Phase Transition
CFD	Computational Fluid Dynamics
FDS	Fire Dynamic Simulator
AGA	American Gas Association
SFM	Solid Flame Model
SEP	Surface Emissive Power
RANS	Reynolds Averaged Navier – Stokes
LES	Large Eddy Simulation
DNS	Direct Numerical Simulation
EDC	Eddy Dissipation Concept
SGS	Sub Grid Scale
HRR	Heat Release Rate
HRRPUV	Heat Release Rate Per Unit Volume
FFT	Finite Fourier Transform
MEM	Maximum Entropy Method

TABLE OF CONTENTS

Page

Page

LIST OF FIGURES

Page

LIST OF TABLES

Page

1 INTRODUCTION

1.1 Liquefied Natural Gas (LNG) background

Liquefied Natural Gas (LNG) is an odorless, clear, non-corrosive liquid at cryogenic temperatures. It is a growing commodity used all over the world. LNG is a mixture of light hydrocarbons which mostly consist of methane (>85%, depending on the type of natural gas used for processing) liquefied to facilitate clean energy source and cost effective transportation of energy across different regions of the world.

Gas production and gathering, liquefaction of gas and storage, transportation and regasification are the four crucial steps in LNG production chain. [25] After removal of acid gas, dehydration, natural gas is liquefied by cooling the gas to its boiling point, -262^0F (-163^0C). This increases the density from around 0.7 kg/m^3 to around 425 kg/m^3. This reduction in volume by a factor of 600 and increase in fuel per unit volume makes LNG convenient for transportation. However, storage at cryogenic temperatures is required to maintain the liquid phase. Therefore, LNG is stored in double-walled tanks with cryogenic nickel/steel inner tank surrounded by outer shell of insulated or pre-stressed concrete.[25] Transportation of LNG is carried out in four types of double hulled ships, viz. Membrane type, Moss type, IHI SPB type and Cylindrical type, each having its own economic and structural advantages.[25] Transfer of LNG from LNG tankers to storage tanks at regasification terminals is done by several unloading arms. Once the LNG is ready to be regasified, it is passed through vaporizers which warms the gas to 5^0C by using seawater, air, natural gas or external heat source. [25]

As explained by Institute of Gas Technology, LNG transportation is more economical than natural gas after 700 miles of offshore distance and 2000 miles onshore transportation.[17]

1.2 Hazards of LNG

LNG, being primarily methane, is flammable in its vapor form. The cryogenic temperature at which the LNG is stored may pose hazards due to extremely low temperatures. High density of LNG can also result in hazards associated with volume expansion. Understanding these hazards is necessary because they could lead to a potential mishap at any point in the life cycle of LNG industry. Hazards associated with LNG can be broadly classified into three types based on its characteristics.

1.2.1 Low temperature hazards

LNG can displace oxygen in the air if the vapor concentration is more than 28%. The oxygen concentration may drop below 15% which can be fatal for breathing causing asphyxiation. Higher concentration of LNG can further displace oxygen with higher threats like vomiting or even death if the concentration is as high as 71%. However, such a scenario is observed only near the release/leak source.[60]

Freeze burns can be another possible hazard due to cryogenic temperature of LNG. Although there has been only one reportable incident of freeze burn in 1977 where an aluminum valve failed and 1500 m^3 LNG spilled on the worker. [11]

1.2.2 Liquid expansion hazards

Rapid Phase Transition (RPT) is a characteristic phenomenon where the cryogenic LNG rapidly vaporizes to vapor. Localized overpressure is created due to rapid and spontaneous vaporization. This is possible when LNG spills on water. The magnitude of energy release is 1780 times less than methane combustion on per unit mass basis and thus, the overpressures are assumed to be negligible and localized during risk assessments.[41]

Roll over hazard[60] can cause complete tank failure. Temperature of the bottom layers in an LNG tank rise due to hydrostatic pressure. Boil off from upper layer may eventually lead to accumulation of heavier components raising the density of the top layers. Inversion of layer may follow the density increase. The lighter hydrocarbons at the bottom rising to the top due to inversion of layers may flash due to sudden release of hydrostatic pressure. The pressure due to large volume of vaporized liquid may exceed the capacity of relief devices, eventually leading to tank failure.

1.2.3 Fire and explosion hazards

LNG spill on land or water will lead to a formation of a liquid pool. Evaporation of the pool will form a flammable mixture over the liquid spill, which upon immediate ignition can lead to a *pool fire*. The heat feedback from the fire will cause more fuel to evaporate until the entire fuel is burnt out.

The delayed ignition of the vapor above the pool may flash back to the pool if the vapor dispersed is not confined in a congested region, causing a *flash* fire. Although it is fatal for people inside the fire, the total radiation on an object resulting from a flash fire is very low as compared to pool fire or jet fire.

Congestion due to equipment such as pipes and pumps can form a high density obstacles, resulting in a potential *vapor cloud explosion*. Detonation explosion of LNG is not possible due to low reactivity (or laminar burning velocity).[60]

Pressurized release of LNG to start a *jet fire* is unlikely since LNG is not stored under high pressure.

1.3 LNG pool fires

When a fuel spills on a horizontal surface, the fuel starts evaporating. The rate at which it evaporates is usually denoted as mass burning flux ($kg/m^2.s$). The mass burning flux of a LNG pool fire (or other fuel) is low and depends on factors such as the diameter and the surface of spill.[60] Since the air is not premixed, combustion takes place only when surrounding air diffuses into the fuel, forms a stoichiometric mixture and ignites.

As the fuel evaporates, it creates a toroidal vortex due to its momentum near the base. This vortex helps in the entrainment of air, causing upward acceleration and creation of low pressure zone behind it. The evaporating fuel occupies this low pressure zone, causing a bulge and a toroidal vortex which tend to stretch the plume outwards. At the same time, the earlier vortex stretches the plume inward. The resulting rotational motion causes more air entrainment with elevation and form larger eddies. Excess stretching of the vortices may cause some of the vortices to separate from the fire intermittently.

The upward motion is due to low density of the fire plume, making the buoyant forces govern the movement of the plume. The density of the plume is around 0.318 kg/m^3[60] and is often neglected for momentum calculations.

1.4 Motivation

The recent “shale-gas revolution” has contributed to almost 50% of the U.S natural gas domestic production in less than a decade.[12] With increase in the number of LNG terminals in the United States of America, there are growing concerns about the hazards posed by LNG import/export terminals and its potential impacts on the public.

Different regulatory bodies in the USA are responsible for ensuring design, environmental, public impacts of such facilities. Federal Energy Regulatory Commission (FERC) is responsible for licensing of these facilities. National Fire Protection Agency (NFPA) prescribes a standard for production, storage and handling of LNG, NFPA 59A. 49 CFR 193 requires NFPA 59A compliance.[29] Two important hazards to be evaluated to define an “exclusion zone” are

- Determining the worst case potential release of LNG and distance up to which the LNG cloud spread until it reaches ½ LFL.
- Thermal exclusion zones evaluation outside which the thermal radiation from potential fire should not exceed 5kW/m^2.

It is of utmost importance to predict the radiation hazard from the fires to ensure safety of public outside these exclusion zones. Such analysis also helps in better planning for siting and emergency response.

Modeling of pool fires for radiation predictions have been under development since 1970s. Most widely used approach is use of empirical modeling, which is based on the experimental observations of pool fire characteristics. Empirical correlations developed over the years, such as the work of Thomas[53], Ris[51], Raj[1, 46], Becker and Liang[6], Moorhouse[42] and many more, however, simplify the dynamics of pool fire. Such approach, although widely used, is limited due to several parameters such as inability to account for interaction with the surrounding environment. Extrapolation of such models can lead to varying predictions due to its validity against experiments used for their development. FERC[16] reported how change of Surface Emissive power (SEP) in an empirical model, LNGFIREIII, can lead to overestimation of radiation for small scale pool fires while fitting the radiation predictions for large scale fires.

A more robust approach include the use of field models, which consider the underlying physics governing the fires. Pioneering work by Launder and Spalding[28], Bilger[8], Magnussen[30], Rehm and Baum[49] and others established the basis of field modeling approach. Application of these concepts to fire modeling was realized by researchers such as Cox[13], Woodburn[59], McGrattan[37, 38]. Field models have shown promising future for hazard analysis for pool fires.

1.5 Objective

It is important to understand how accurate field model approach describe the dynamics of pool fires. However, every model requires validation against experimental data for its applicability to different scenarios. Thus, this research will address the capability of field model, i.e. Computational Fluid Dynamics (CFD), and validate it against a small scale pool fire, as a step towards better hazard predictions. Objectives of this work are:

- Study small scale pool fires using CFD by looking at the pool fire structure
- Study transient pulsation characteristics of the fire.
- Compare effects of two small scale eddy turbulence models, viz. Smagorinsky model and Deardorff model, on radiation prediction at a distance and the shape of the flame.
- Study different numerical approaches to determine flame geometry such as flame length, height and tilt predicted by FDS.

Experimental data of pool fire experiment performed by a former Mary Kay O'Conner Process Safety Center (MKOPSC) graduate student[21] will be used to fulfill the above objectives. The pool fire was a confined fire in a dike having burning surface area of 1m x 1m.

2 LNG POOL FIRES

The complexity of pool fire discussed in Section 1.3 is condensed into a definition of pool fire by TNO Yellow Book.

"A pool fire is defined as turbulent diffusion fire burning above a horizontal pool vaporizing flammable material under conditions where the flammable material has zero or very low initial momentum."[14]

2.1 Pool fire structure

The pool fire structure is usually simplified into three zones, as shown in Figure 1: Zone 1 being the visible luminous region, Zone 2 being the combustion zone and Zone 3 is the smoky region, where burning may occur intermittently.

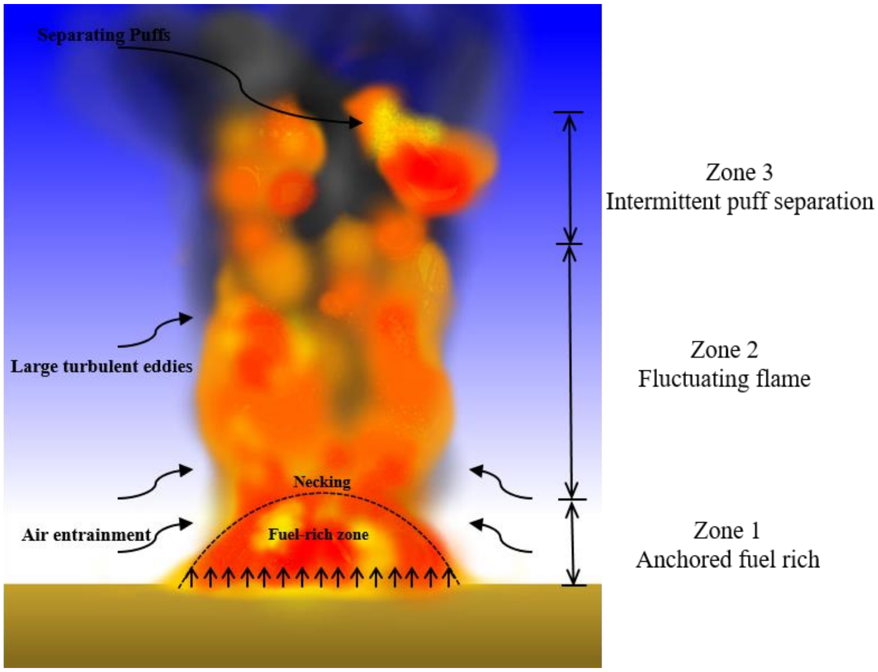

Figure 1: Schematic of pool fire[47]

Luminous Zone 1 is the region which is rich in fuel and in a fire with large diameter, this zone is optically thick.[46] This region is normally 20% of the average flame height or around distance *D/2* to *D* (Diameter) above the base of the fire, relatively cool as small amount of oxygen has penetrated to the center.[20, 47] The toroidal vortex which causes air entrainment is accelerated upward, decreasing the diameter of the plume until a point called as necking point. The height of this zone is almost constant throughout the burning and is anchored to the base of the fire.

The flame in Zone 2 is attached to the luminous zone. As the fuel rises upwards due to buoyancy in a rotational motion, more air is entrained. This causes large eddies of size as big as the diameter.[31] These eddies may have unburnt fuel or partially burnt fuel from Zone 1. Since air in convected radially into the fire, efficient combustion may take place with little formation of intermediates such as carbon monoxide (CO) and soot.[20] This zone is seen from 20-40% of the average flame height.[47]

Zone 3 is a fluctuating region where some fuel/partially burnt fuel with soot or other products may depart from the flame. The separation of these puffs is attributed to excessive stretching of large eddies.[31] Formation of smoke is observed in this region due to reduction in rate of chemical reaction since colder air is entrained and the temperature drops.[20] This region substantially affects the radiation from the fire incident on the surrounding.[46]

2.2 Geometry

The shape of the flame of a pool fire is not steady throughout the burning phase and thus approximation by assuming time-averaged shape is necessary for quantification.

The extents of a pool fire are described by assuming the time-averaged flame takes a cylindrical shape.

Froude number, Fr, is defined as the average of ratio of inertial to buoyant force. Froude number is found to dictate the structure of the fire. Combustion Froude number is the form of Froude number expressed in terms of mass burning flux of the pool fire and the ambient air density[60],

$$F_c = \frac{\dot{m}''}{\rho_a \sqrt{g\, D_e}} \qquad \textbf{(1)}$$

where, $\dot{m}''$=Mass burning flux, $kg/(m^2.s)$

ρ_a = Ambient air density, kg/m^3

D_e = Equivalent pool diameter, *m*.

Early works of Ris [51] and Thomas[53] led to the inception of “Froude number modeling”. Low Froude number mean the buoyant forces are dominant and larger variation of flame boundary with time is observed in the necking-in region.[20] Ambient air density was used by Thomas due to unknown value for the density of wood volatiles during his wood crib fire experiments.[53] Since the density of the plume is very low, neglecting the density of the plume does not affect the desired ratio.[6] Equivalent pool diameter is calculated in case of a pool fire which is not circular in diameter.[14]

$$D_e = \frac{4A_p}{S_p} \qquad \textbf{(2)}$$

where A_p is the pool surface area and S_p is the perimeter of the pool.

2.3 Flame length

Flame length of the pool fire is considered as the visible luminescent flame. Visual observation of average flame height is usually taken as the flame height. However, Zukoski and Cetegen[63] proposed objective way to determine flame height. It is the height where at least part of the flame is above the horizontal plane at an elevation, z above the burning surface, 50% of the time. Heskestad[22] based on the data from Zukoski et al., proposed that the length to diameter ratio is dependent on non-dimensional group, N, which is expressed in the form of total heat release rate of the fire.

$$N = \left[\frac{C_p T_a}{g \rho_a^2 (H_c/r)^3}\right]\left(\frac{Q^2}{D^5}\right) \tag{3}$$

$$\frac{L}{D} = -1.02 + 15.6 N^{\frac{1}{5}} \tag{4}$$

where, $Q = \dot{m} H_c$ = Total heat release rate, W

H_c = Heat of combustion per unit mass, *J/kg*.

$\dot{m}$ = Mass burning rate, *m/s*.

$D = \sqrt{4A_p/\pi}$ = Effective diameter of the pool, m

r = stoichiometric mass ratio of air to volatiles

T_a = Temperature of ambient air, K

C_p = Specific heat capacity of ambient air, *J/(kg.K)*

L = Flame length, m

Thomas[53] based on the wood crib fire experiments in 1963, proposed that length to diameter ratio is proportional to the combustion Froude number. A modified equation included the effect of wind on the flame length.

$$\frac{L}{D_e} = AF_c^p(U^*)^q \tag{5}$$

where U^* is the dimensionless wind speed given as,

$$U^* = \frac{U_{wind}}{\left[\frac{\dot{m}''}{\rho_a} gD\right]^{1/3}} \tag{6}$$

The constants A, p and q are suggested to be 42, 0.61 and 0 respectively by Thomas for the Froude number between 10^{-2} and 10^{-1}. Modified equation suggested the use of 55, (2/3) and -0.21 respectively, to take into account the effect of wind on the flame length.[53] Moorhouse[42] suggested the values 6.2, 0.254 and -0.044 for A, p and q respectively based upon curve fitting for an LNG fire test series.

The flame height is the vertical height from the base of the fire, when the flame tilts due to the wind.

2.4 Flame tilt

The flame tilt is considered as the angle made by flame centerline with the vertical. American Gas Association (AGA) [1] developed a correlation for estimating the flame tilt, θ, which relates the tilt with the non-dimensional wind speed given in equation (6).

$$\begin{aligned} cos\theta &= \frac{1}{\sqrt{u^*}} for\ u^* > 1 \\ &= 0\ for\ u^* \leq 1 \end{aligned} \tag{7}$$

Welker and Sliepcevich [58] also developed a correlation for the tilt as a function of ratio of density of fuel vapor to ambient air, Reynold’s number and Froude number.

However, the Welker and Sliepcevich correlation is insensitive to wind speed as wind velocity is related only through Reynolds number which has a very low power dependence of 0.07.

2.5 Fire characteristics

Fire characteristics indicate the inherent characteristics of the pool fire that affect the physical aspects of the fire. Radiation from pool fire is a complex phenomenon due to the turbulent nature of the fire. Owing to the non-linearity of the Planck's law, small uncertainties in temperature estimation disseminate into large radiation estimation uncertainties. Atmospheric absorption adds further to this uncertainty.[20]

2.5.1 Mass burning rate

Mass burning rate is expressed in terms of regression rate, m'' *(kg/s),* or burning flux, $\dot{m}''$ *(kg/m²s).* Burning flux is the product of regression rate and the density of liquid. Burning flux can be estimated theoretically by using the following equation,[60]

$$\dot{m}'' = \frac{10^{-3}\Delta H_c}{\Delta H_v^*} \qquad \textbf{(8)}$$

Here, ΔH_c is the heat of combustion of the fuel, *J/kg*, and ΔH_v^* is the modified heat of vaporization, *J/kg*, which includes the heat required to raise the temperature of the fuel to its boiling point. Heat of combustion of LNG vary from 50MJ/kg to 55MJ/kg. [15]

Estimation of mass burning rate was represented by using an empirical non-linear curve fitting correlation,

$$\dot{m}'' = \dot{m}''_{\infty}\left(1 - e^{-\kappa\beta D}\right) \qquad \textbf{(9)}$$

Here, κ is the absorption coefficient, m^{-1}, β is mean beam length corrector and D is the effective pool diameter. Babraskaus[4], based on the above correlation developed by Zabetakis and Burgess[10] suggested values for $\dot{m}''_{\infty}$, κ and β for different fuels.

2.5.2 Surface Emissive Power (SEP)

The radiant energy flux emitted from the fire is characterized by the Surface Emissive Power (SEP), W/m^2. The mean SEP of a fire is measured using Wide Angle Radiometer (WAR) and correction for atmospheric interference and view angle of WAR is applied.[60]

The SEP of a flame can be estimated by using the

$$E = SEP = SEP_{max}(1 - e^{-\kappa D}) \qquad \textbf{(10)}$$

where, SEP_{max} = Maximum Surface Emissive Power, $\frac{kW}{m^2}$

κ = Extinction coefficient, m^{-1}

D = Pool diameter, m

The extinction coefficient or attenuation coefficient is inverse of the optical depth of the fire, which is found to be approximately equal to pool diameter for small diameter fire.[60] The SEP_{max} is either obtained from experiments by using WAR or is estimated by assuming the flame surface to be a black body emitter.

$$SEP_{max} = \sigma T_F^4 \qquad \textbf{(11)}$$

The SEP averaged over the flame surface uses the dimensions of the cylinder describing the flame obtained from empirical correlations as described in Section 2.2. Equation (11) assumes that the fire is a black body emitter. However, Malvos and Raj[32] showed that the fire is a band emitter of radiation and not a continuous emitter. Large radiation decrease is observed during the CO_2 and water vapor absorption bands in Infrared (IR) region of the spectrum.

Becker and Liang[7] showed large dependence of soot yield on Richardson number, the ratio of buoyancy of flame to momentum flux of the source. Methane pool fires were observed to be non-sooty at small diameters, and carbon monoxide yield was unrelated to the soot yield, unlike expected.[27] Effect of soot formation on SEP was reported during several large scale experiments. Notorianni et al.[44] studied the soot mass fraction yields for crude oil fires, ranging from 0.053m to 17.2m effective diameter. Soot yield (Y), in terms of mass, *kg*, formed per unit mass of fuel burnt, is correlated to the pool diameter by Raj[46] based on the soot yield data from Notrianni.

$$Y = 9.412 + 2.758 \log_{10} D \tag{12}$$

2.5.3 Flame pulsation

Shedding of vertical structures by the flame is an inherent property of pool fire. Flame bulges observed due to buoyancy and volume expansion due to combustion above the surface of the pool fire propagate downstream. This causes the flame length to vary with time.[20] This oscillatory behavior of the flame is called ‘puffing’ phenomenon.

The frequency of oscillation, as shown by Hamins[20], McCaffrey[34] and other researchers, vary proportionally to inverse square root of pool diameter. Malalasekara and Versteeg[31], based on the experiments of burner diameter ranging from 0.05 m to 0.14 m for propane fuel and data from previous studies, proposed a correlation for predicting pulsation frequency for different effective pool diameter.

$$f = \frac{1.68}{\sqrt{D}} \tag{13}$$

Where f is the frequency of oscillations in Hz. Tieszen et al. performed experiments to measure the puffing frequency of a 1 m diameter pool fire.[54] The puffing frequency measured by using PIV technique was 1.64 Hz, which is close to the frequency predicted by the above empirical equation.

2.6 Pool fire modeling

Prediction of radiation from the pool fire is an important part of the hazard analysis. Pool fire models can be broadly classified into three types.

a) Semi Empirical Models – Developed using experimental data and mostly involve empirical correlations for defining pool fire characteristics. Their application may be limited due to specific type of experiments through which they were developed.

b) Integral models – They include underlying principles of Physics thus can be used for wider range of scenarios. The accuracy and computation of such models lie between the empirical models and the field models. However, no such model exist for pool fire.[14]

c) Field Models – Complex models which form the solution to partial differential equations governing the conservation of mass, momentum and energy for accurate representation of real life fire.

2.7 Point source model

Point source model is the simplest semi-empirical model for predicting the thermal radiation from the fire. It assumes that all the radiation from the fire originates from a point source and uniform radiation at an imaginary hemisphere, radial distance, *x*, from the point is estimated by the following equation.[60] Figure 2 shows schematic of Point Source model.

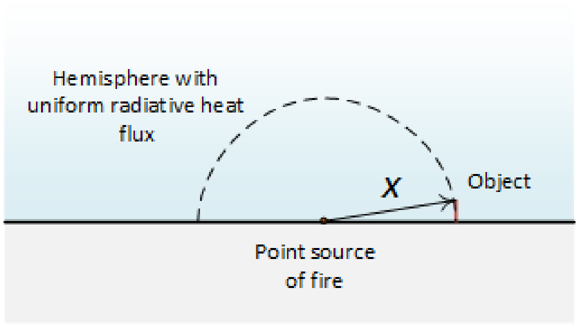

Figure 2: Schematic of point source model

$$E(x) = \frac{\chi_r Q}{4\pi x^2} = \frac{\chi_r A_p \dot{m}'' \Delta H_c}{4\pi x^2} \tag{14}$$

where $E\ (x) =$ Radiant energy flux incident from the point source at distance $x, kW/m^2$

χ_r = Fraction of combustion energy radiated from the fire.

In reality, the fire emits energy from its surface and not just a point, so such representation of fire could be practical if the radiant heat is to be found in far – field. Raj[48] suggest use of point source model with precaution and only if

- Radiation fraction of the fire is known.
- Radiation level of interest at a distance *x* is low (1 – 5 kW/m^2)
- Equivalent diameter of fire is small (D<5m)

2.8 Solid flame model

Solid Flame model is a more in-depth semi-empirical model than point source model. The fire is represented as a cylinder. The thermal radiation received by an object at distance, *d*, can be expressed as,

$$q_r'' = EF\tau_{atm} \tag{15}$$

where, E = Surface Emissive power of estimated cylindrical surface of the fire.

F = View factor of the object at distance *d*.

τ_{atm} = Transmissivity, function of distance and relative humidity

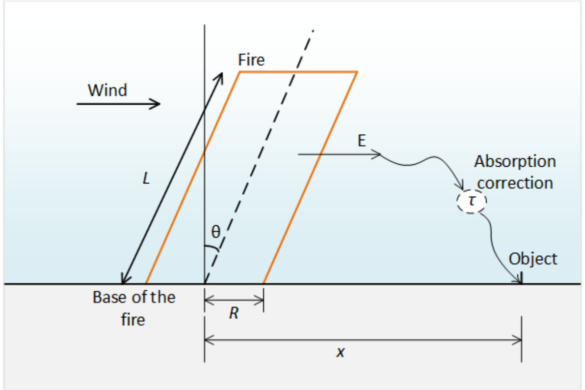

Figure 3: Schematic of solid flame model

Schematic of Solid Flame model is given above in Figure 3. LNGFIREIII[3], developed by Gas Research Institute and POOLFIRE6[50], developed by Rew and Hulbert, are examples of solid flame model used as a part of regulatory purposes.

Correlations used in LNGFIREIII will be used in this study. The SEP, *E*, is modeled using the equation (10) with attenuation coefficient, κ, as 0.3 m^{-1}, and SEP_{max} for pool fires on land as 190kW/m^2. [16] Experimental data indicate variation of SEP from

20 kW/m^2 to 300 kW/m^2. Sandia National Laboratory Phoenix test series suggested SEP during the 56m pool fire experiment had an uncertainty range of 248-326 kW/m^2. [9] MKOPSC white paper[33] lists all the recommended changes by Sandia National Laboratory and other research groups. Comparison with Montoir test (35 m land based pool fire), indicated under prediction of SEP when SEP_{max} is considered 190kW/m^2. Increasing SEP_{max} to fit the Montoir test data will result in much more conservative results for small scale fires.[16, 43]

As shown by Raj[46], **length** correlations used to determine mean SEP from experimental data should not be changed for hazard assessment from pool fires of different size as it may lead to significant deviations. LNGFIREIII uses Thomas correlation, equation (5) with A=42, p=0.61, q=0.[3]

Atmospheric transmissivity, τ, is important due to significant absorption from CO_2 and water vapor in the infrared spectrum as described earlier in section 2.5.1. LNGFIREIII neglects the effect of CO_2 absorption.[3]

$$\tau = 1 - \alpha_w \qquad (16)$$

where α_w is transmissivity due to water vapor, which is a function of relative humidity and vapor pressure of saturated water vapor. The equations used for calculating absorption from water vapor are shown in Appendix A.

View Factor, *F*, is obtained by considering either cylindrical or rectangular shape of the fire. In case of cylindrical tilted fire, the tilt angle, θ, obtained from equation (7), is positive for target downwind and negative for upwind target. Vector sum of horizontal and vertical view factors is taken to determine maximum view factor.

$$F_{max} = \sqrt{F_v^2 + F_h^2} \qquad (17)$$

where F_v and F_h are vertical and horizontal view factors respectively. Equations to determine F_v and F_h are shown in Appendix A

LNGFIREIII uses empirical correlation as described in equation (9)[3] for estimating **mass burning flux**. For circular diameters, m''_{∞} is taken as 0.11 kg/m^{2}s and the $\kappa\beta$ value as 0.46. This value is based on pool fires of diameter ranging from 0.15m to 20m.[16]

A correlation for rectangular fires used in LNGFIREIII relates aspect ratio (AR) defined as ratio of length to width, and modified Froude number.[3]

$$\begin{aligned} \dot{m}'' &= 0.043 + 0.068(AR.Fr)^{0.872} && \text{if } AR.FR>1 \\ \dot{m}'' &= m''_{max} && \text{if } AR.FR\leq 1 \end{aligned} \qquad \textbf{(18)}$$

Estimation of flame **tilt** is done in LNGFIREIII by A.G.A correlation, shown by equation (7), with wind speed at desired elevation obtained from power law, to include Pasquill stability class.[3]

Raj developed a probabilistic approach for describing this variability of SEP with height which predicts the SEP along the height to be in agreement within the uncertainty of measurements of Montoir test.[46]

2.9 Field models (Computational Fluid Dynamics)

Computational Fluid Dynamics (CFD) is an advanced computational method which solves the problem by using underlying principles of conservation. Pool fires, being buoyant turbulent diffusion flames, need inclusion of turbulence modeling, radiation and combustion for accurate predictions. Field models consider interactions with surrounding environment and could be modeled for irregular shaped pool fire. [23]

2.9.1 Turbulence

Random structure of turbulent flows is attributed to eddy which have wide ranges of length, time and velocity scales. The large eddies, which are dominated by inertial forces than viscous forces (Re>>1), extract energy from the mean flow causing eddies to stretch, a phenomenon called as 'vortex stretching'. Small eddies are stretched due to comparatively larger eddies. This results in the kinetic energy being 'cascaded' to smaller eddies. The fluctuating properties have energy across a range of wavenumbers ($\kappa = 2\pi/l$, l is the length scale of eddies).

Spectral energy, $E(\kappa)$, a function of wavenumber, κ, decreases as the wavenumber increases, indicating that smallest eddies (large wavenumber) have lowest energy. Smallest eddies, having the length scale ranging from 0.1 to 0.01 mm and frequencies of about 10kHz, are dominated by viscous forces and the Reynolds number based on their length and length scale is 1. The work is performed against viscous stresses at these small scales, and thus the energy is dissipated in the form of thermal energy.

Large scale eddies are dominated by inertial forces and their spectral energy content, $E(\kappa)$, is proportional to $\upsilon^2 l$ (υ is velocity scale and l being the length scale). Large scale eddies are anisotropic (variating fluctuations in different directions) as the length scale depends on turbulence producing properties like the obstacle length, roughness of surface.

On the other hand, small scale eddies, suggested by Kolmogorov, depend only on rate of dissipation of turbulent energy ε (m^2/s^3), are isotropic as directional diffusivity of viscosity do not exist at the length scale of small eddies.[57]

2.9.2 Turbulence modeling

Solving Navier – Stokes equation to assess all the eddy scales need the spatial and temporal distribution to be at the scale of length, time scale of smallest eddies in order to accurately obtain the behavior of the flow, both of which being very small, would be computationally very expensive due to large time and memory requirements.

Turbulence modeling approaches can be classified into three types, each of which have characteristic way/s to model turbulence and small scale eddies.

a) Reynolds Averaged Navier – Stokes (RANS) – This approach uses the principle of describing the fluctuating property, φ, as summation of mean value (Φ) and fluctuating component (φ'). Time averaging the Navier – Stokes equation give rise to time averaged equations of conservations which contain extra turbulent stresses called as Reynolds stresses. The mean flow is solved and these extra turbulent stresses are solved using different approaches, κ-ε two equation model being one of them. κ is the turbulent kinetic energy and ε is dissipation rate of turbulent kinetic energy.[57]

b) Large Eddy Simulation (LES) – This approach applies spatial filtering to the Navier – Stokes equations and the resulting equations can resolve the interactions between all eddies having length larger than the spatial filter. Effect of eddies smaller than the filter width are modeled using sub grid scale (SGS) models, Smagorinsky SGS model being one of them.[57]

c) Direct Numerical Simulation (DNS) – This approach is direct numerical solution of Navier – Stokes equations by using fine spatial mesh and temporal steps sufficient enough to accurately describe the smallest eddies in the flow. Huge computation time and power is required to solve for such a small time and length scale.[57]

Figure 4 shows a graphic of energy cascade to smallest eddies and different approaches of turbulence modeling.

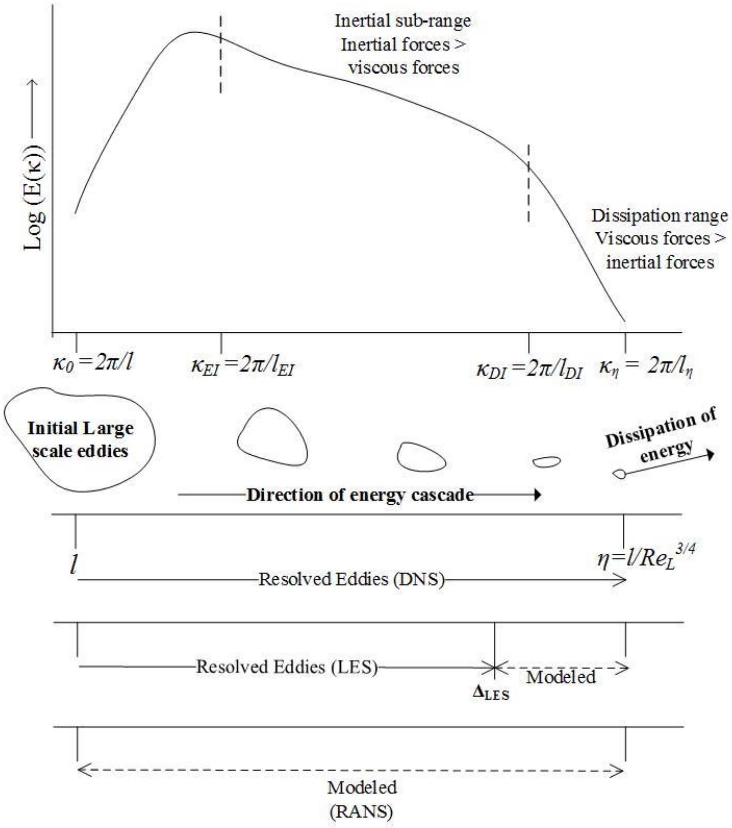

Figure 4: Energy cascade and different CFD approaches

RANS does not solve any scale of turbulence, while LES resolves large scale eddies.[57] Since buoyancy plays an important role in describing pool fires, the large density variation due to temperature result in increased turbulence. The turbulent rotational characteristics of a fire are lost due to isotropic assumption for all eddies in RANS approach. However, LES solves directly for the turbulent anisotropic eddies present in the fire. Thus, LES provides deeper insight into the time varying phenomenon inside the fire, making it a promising future for fire modeling.[57] Therefore, LES was the choice of approach for this study.

2.9.3 Commercial software

Flame ACcelator Simulator (FLACS) is developed, maintained and supported by Christian Michelsen Research (CMR) since 1992. FLACS uses RANS methodology and κ-ε model for describing turbulence.[18] FLACS-Fire uses Eddy Dissipation Concept (EDC) for combustion and ray tracing model for radiation transport.

Kameleon (KFX), owned by ComputIT, is another CFD model which uses κ-ε model.[56] Ansys FLUENT, is another licensed CFD solvers which have wide range of turbulence models to choose for RANS and LES, and uses grey gas and spectral radiation solver.[2] OpenFOAM [19], an open source software, has flexibility to select from LES and RANS methodology with range of turbulence models.

Fire Dynamic Simulator (FDS), an open source tool developed for low Mach number, thermally driven flows by National Institute of Standard and Technology (NIST), uses LES methodology and the version 6 uses default Deardorff model for describing turbulence.[40] FDS, like FLACS, also uses EDC to describe combustion, but uses Grey Gas assumption or 6 band model for radiation transport.

FDS, developed specifically for describing low speed fires governed by buoyancy, has been validated against small scale pool fires and is gaining importance in application in industries.[35] Thus, FDS was selected for study during this project.

2.10 Previous relevant research

Rehm and Baum in 1978[49] developed governing equations for thermally driven buoyant flows. These equations called as low Mach number equations form the basis of the Large Eddy Simulation (LES).

McGrattan, with Rehm and Baum, in 1994[37], first used these equations for transient 2D simulation to track smoke species on an inclined surface. Baum[5], in 1997, used same equations for 3D transient plume simulation. Lagrangian approach, where large number of particles introduced in the domain are convected due to buoyancy. The heat release rate of these particles was given as a constant heat source. These two works led to the inception of LES in modeling of fire.

Similar LES approach used by Baum and McGrattan along with other models such as mixture fraction combustion model and radiation model was incorporated in the open source software Fire Dynamic Simulator (FDS) in 2000[39].

Hostikka and McGrattan[24], in 2003, studied the radiation transport for methane fire of diameter ranging from 0.1 m to 1 m using the 6 band model and single wide band model. The heat fluxes are highly over predicted for higher mass burning flux (4 g/m^2.s) for lower diameter (0.1 m) and low burning flux (3 g/m^2.s) for 1 m diameter. The rest of the heat flux is in good agreement with the experimental values and the 6 band model is sufficient for radiation transport. Owing to this accuracy of the six band model and more realistic division into smaller bands, six band model will be used for this study.

Xin et al.[62], in 2005, performed FDS simulation for 7.1cm methane pool fire and compared the experimental measurements with horizontal and vertical velocity, and temperature. Temperature was compared for validating the mixture fraction model for describing buoyant flames. Temperature predictions near the burner exit were over-predicted (~500 K), but temperature was in agreement further downstream of the burner.

Xin et al.[61], in another research work in 2008, performed similar validation work for 1m methane pool fire simulated at the FLAME facility in New Mexico and compared the results with experiments performed by Tieszen[54] for validating puffing frequency predictions and turbulent characteristics predicted by FDS5.

LES was used later for predictions of Surface Emissive Power (SEP) from the fire such as the work of Schälike[52].

Constant coefficient Smagorinsky turbulence model is the most widely used turbulence approach. However, Smagorinsky model is dissipative[45] due to its dependence on mean resolved strain rate of turbulent flow. Even with the fine mesh, the modeled turbulence does not decrease because of its dependence on mean strain. This is avoided by case by case assessment of Smagorinsky coefficient or with the use of dynamic Smagorinsky model which adjusts for these changes based on the local flow conditions.[57]

Adrian Kelsey[26], in 2014, performed a global sensitivity which involved sensitivity of pool fire characteristics on turbulence model. The Deardorff turbulence model and constant Smagorinsky model were studied to find that the pool fire geometry such as height is affected by the turbulence model used. The entrainment rate was concluded to be severely affected.

Deardorff model derived from Prandtl mixing length model assumes dependence of Deardorff model on sub-grid kinetic energy[31, 36], thus, smaller mesh sizes result in less energy dissipation to smaller turbulent scales.

A more recent study by Yujie Lin[1] in Mary Kay O'Conner Process Safety Center (MKOPSC) performed simulation of 1m x 1m pool fire for validation study for the small scale pool fire using Deardorff model.

---

[1] *Yujie Lin, Depeng Kong, Monir Ahammad, M.Sam.Mannan*,, Use of FDS for the prediction of medium-scale LNG pool fires. This paper has been submitted to Journal of Safety Health & Environmental Research at the time of writing this document.

3 DESCRIPTION OF EXPERIMENT

A small scale experiment was conducted at Brayton Fire Training Field (BFTF) in December 2009 by Carolina Herrera, a former graduate student of Texas A&M University.[21] The experiments were conducted to simulate pool fire on land and the pool was restricted by a concrete dike. The LNG composition was about 99.5% for this test.[21] The dimensions of the pool formed in the dike was 1m x 1m x 0.2m. Objective of this experiment was to measure parameters such as temperature, liquid level, evaporation rate, radiative heat, atmospheric conditions to study mass burning rates. Instruments used to do so are described below in Table 1.

Table 1: Instrumentation used in the experiment[21]

Equipment/Instrument	Function	Comments
Thermocouples at 0.5” separation until 19” above the center of the pool	Measure liquid regression rate, flame temperature	Higher of 4% or ±1.1 ^{0}C uncertainty of measurement.
Four radiometers with two located away from fire at different locations and two above the fire at different heights.	Radiative heat flux and radiative feedback	±3% uncertainty of measurement, view angle of 150^0.
Differential pressure transducer	Measure change in liquid level	Very small uncertainty

All the measurements were recorded every second, except for the weather stations which recorded ambient conditions every minute at elevation of 2m. The schematic of layout of the radiometers away from the pool is shown below.

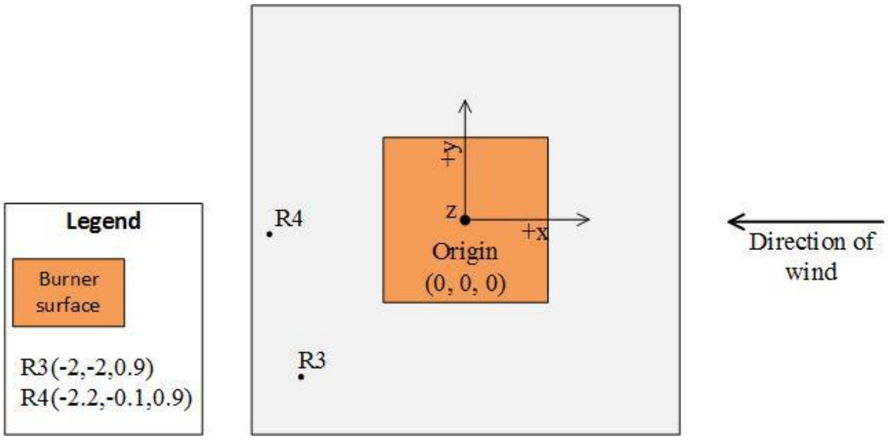

Figure 5: Schematic of setup of experiment.

Three tests were performed and only the third test was selected for the present study. Third test was chosen due to negligible solar radiation and wind direction. The wind direction was perpendicular to length of the dike (as shown above), making it easier for its setup in FDS. Ambient conditions used for the simulation are shown below in Table 2.

Table 2: Ambient conditions for experiment[21].

Temperature (C)	Average wind speed (m/s)	Wind direction	Relative humidity (%)
7.2±0.12	0.5±0.35	S	55.16±0.93

4 METHODOLOGY USING FDS

This section describes models used for present study for the simulation and brief methodology used for determining different parameters. The Experiment described in Section 3 has been simulated with the help of a methodology as described below. A uniform staggered grid of cubic cells is used in FDS version 6.3.2 for all the simulations. A mesh sensitivity study was performed. This was done by looking at the effect of mesh size on temperature, velocities, oxygen and methane mass fraction above the fire at the center.

The radiation solver used for this study is finite volume method for Radiation Transport equation (RTE). Finite Volume Method uses approximately 100 discrete angles to discretize the complex radiation transport equation[36]. 6 band model is used so that absorption due to water vapor and carbon-di-oxide are considered in their respective dominant infrared bands.

4.1 Turbulence and combustion models

FDS uses filter width of size equal to the cube root of the volume of the cell, $\Delta = V_c^{1/3}$ where V_c is the volume of the control volume. The filter is applied to the transport equations to obtain the LES equations for mass, momentum and energy. When the filter is applied to a continuous field, Φ, the filtered field can be expressed as

$$\overline{\Phi}(x,y,z,t) = \frac{1}{V_c}\int_{x-\delta x/2}^{x+\delta x/2}\int_{y-\delta y/2}^{y-\delta y/2}\int_{z-\delta z/2}^{z-\delta z/2}\phi(x',y',z',t)\,dx'dy'dz' \qquad \textbf{(19)}$$

This filtering process gives set of N-S equations which is solved numerically to resolve the turbulence of scales higher than the filter size. The turbulent eddies of scales smaller than the filter size are modeled using turbulence models. Only details of combustion model and conservation of momentum and details of other models can be found in FDS Technical Reference Guide.[36]

4.1.1 Conservation of momentum

Conservative form of momentum equation is expressed as,

$$\frac{\partial \rho u_i}{\partial t} + \frac{\partial\left(\rho u_i u_j\right)}{\partial x_j} = -\frac{\partial p}{\partial x_i} - \frac{\partial \tau_{ij}}{\partial x_j} + \rho g_i \tag{20}$$

LES filter as shown in equation **(19)**, is applied to equation **(20)** to obtain the LES momentum equation

$$\frac{\partial \overline{\rho u_i}}{\partial t} + \frac{\boldsymbol{\partial\left(\overline{\rho u_i u_j}\right)}}{\boldsymbol{\partial x_j}} = -\frac{\partial \bar{p}}{\partial x_i} - \frac{\partial \overline{\tau_{ij}}}{\partial x_j} + \bar{\rho} g_i \tag{21}$$

The term $\overline{\rho u_i u_j}$ cannot be computed in time directly. A Favre filter, equation (22) needs to be used.

$$\tilde{u} = \frac{\overline{\rho u}}{\bar{\rho}} \tag{22}$$

Favre averaging method is based on density weighted averaging procedure. This reduces the extra terms arising from use of Reynolds decomposition of variables.[57] The instantaneous velocity in terms of Favre average is given as

$$u = \tilde{u} + u'' = \frac{\overline{\rho u}}{\bar{\rho}} + u'' \tag{23}$$

Unlike Reynolds decomposition, the term $u"$ also includes effect of density, and is equal to u' and $\tilde{u} = \bar{u}$ if the flow is incompressible. Similar to characteristics of Reynolds decomposition, $\overline{u"} = 0$ or $\overline{\rho u"} = 0$, thus the term $\overline{\rho u_i u_j}$ can be decomposed as

$$\overline{\rho u_i u_j} = \overline{\rho(\widetilde{u_i} + u_i")(\widetilde{u_j} + u_j")} = \bar{\rho}\widetilde{u_i}\widetilde{u_l} + \overline{\rho u_i" u_j"} \qquad \textbf{(24)}$$

The term $\overline{\rho u_i" u_j"}$ is the sub-grid stress which can be expressed as equation **(25)**, is substituted in equation **(21)**.

$$\tau_{ij}^{sgs} = \bar{\rho}\left(\overline{u_i u_j} - \widetilde{u_i}\widetilde{u_l}\right) \qquad \textbf{(25)}$$

$$\frac{\partial \bar{\rho}\widetilde{u_i}}{\partial t} + \frac{\partial(\bar{\rho}\widetilde{u_i}\widetilde{u_l})}{\partial x_j} = -\frac{\partial \bar{p}}{\partial x_i} - \frac{\partial \overline{\tau_{ij}}}{\partial x_j} - \frac{\partial \tau_{ij}^{sgs}}{\partial x_j} + \bar{\rho} g_i \qquad \textbf{(26)}$$

Once sub-grid stress τ_{ij}^{sgs} is computed, all variables in the equation **(26)** can be computed. This closure is done by applying Newton’s law of viscosity (or Boussinesq approximation) as a constitutive relationship for the entire viscous stress which can be written as,

$$\tau_{ij}^{dev} = \overline{\tau_{ij}} + \tau_{ij}^{sgs} - \frac{1}{3}\tau_{kk}^{sgs}\delta_{ij} = -2(\mu + \mu_t)\left(\widetilde{S_{ij}} - \frac{1}{3}(\nabla . \tilde{u})\delta_{ij}\right) \qquad \textbf{(27)}$$

where δ_{ij} is the Kronecker delta ($\delta_{ij} = 1$ if $i = j$, $\delta_{ij} = 0$ if $i \neq j$)

$\mu_t = \text{Turbulent viscosity}$

$$\widetilde{S_{ij}} = \frac{1}{2}\left(\frac{\partial \widetilde{u_i}}{\partial x_j} + \frac{\partial \widetilde{u_j}}{\partial x_i}\right)$$

This turbulent viscosity, μ_t (Pa.s), is modeled using turbulence models. Two turbulence models are described below. Both the models mentioned below for calculating SGS Reynolds stress are based on Boussinesq eddy viscosity hypothesis which assumes that the change of resolved flow takes place slow enough for the SGS eddies to adjust instantaneously to the rate of strain of the resolved flow. [57]

A. Constant coefficient Smagorinsky model

The Smagorinsky model is based on the Prandtl's mixing length model and assumes that the kinematic SGS viscosity, $\upsilon_t, (\ m^2/s)$, can be expressed in terms of length and velocity scale.[57]

The size of the SGS eddy is determined by the filter width, which in case of FDS is $\Delta = V_c^{\frac{1}{3}} = (\delta x \delta y \delta z)^{\frac{1}{3}}$. Thus, the length scale, according to Smagorinsky theory, is the filter width.

The velocity scale, ϑ, is expressed as the product of length scale and average rate of resolved strain, $|S|$

$$\upsilon_t = C_s l \vartheta \tag{28}$$

$$\vartheta = C_s \Delta |S| \tag{29}$$

$$\mu_t = \rho (C_s \Delta)^2 |S| \tag{30}$$

where, C_s is Smagorinsky Constant, and resolved strain is written as,

$$|S| = \left(2 S_{ij} S_{ij} - \frac{2}{3} (\nabla . u)^2\right)^{\frac{1}{2}} \tag{31}$$

Default value of C_s is 0.2 in FDS. Lilly[57] suggested the value between 0.17 and 0.21. The difference in C_s is attributable to effect of mean flow strain or shear, suggesting a case-by-case assessment of its value for specific scenario. The drawback of Smagorinsky model is that it is dissipative.[57] The modeled eddies are dependent on resolved strain rate and thus finer mesh does not lead to disappearance of this term.

B. Deardorff model

The Deardorff model also called higher-order SGS model considers the length scale same as the filter width, Δ, similar to the Smagorinsky model. However, the velocity scale is considered as square root of SGS turbulent kinetic energy.[35]

$$\upsilon_t = C_\upsilon \mathrm{l}\vartheta \qquad \textbf{(32)}$$

$$\vartheta = \sqrt{\kappa_{sgs}} \qquad \textbf{(33)}$$

$$\mu_t = \rho C_\upsilon \sqrt{\kappa_{sgs}} \qquad \textbf{(34)}$$

where, $\kappa_{sgs} = \frac{1}{2}((\bar{u} - \hat{u})^2 + (\bar{v} - \hat{v})^2 + (\bar{w} - \hat{w})^2)$

$\bar{u}$ = average value of *u* at the center of the grid cell

$\hat{u}$ = weighted average of *u* over adjacent cells

The value of C_υ is 0.1 in FDS.[35] The velocity scale used for this model represents the velocities of small scale turbulent eddies rather than the its dependence on the mean flow.[57]

4.1.2 Combustion

FDS uses lumped species approach to track each of the modeled species. Table 3 shows example of lumped and primitive species used by FDS for single combustion reaction of methane, which is represented by Equation (35).

$$9.52(0.21O_2 + 0.79N_2) + CH_4 \rightarrow 10.52(0.095CO_2 + 0.19H_2O + 0.715N_2) \quad \textbf{(35)}$$

Table 3: Lumped and primitive species.

Lumped Species (Z_α=mass fraction of α)	Primitive Species (Y_α= mass fraction of species α)
Fuel (F)	CH_4
Air (A)	O_2,N_2
Products (P)	CO_2, H_2O, N_2

Transport equation for all but one less primitive species has the form of

$$\frac{\partial(\rho Z_\alpha)}{\partial t} + \nabla.(\rho Z_\alpha u) = \nabla.(\rho D_\alpha \nabla Z_\alpha) + \dot{m}_\alpha''' \quad \textbf{(36)}$$

where Z_α = mass fraction of lumped species,α

$\dot{m}_\alpha'''$= mass production rate of species, α. *(kg/ (m^3.s))*

D_α=Diffusivity of species, α

The mass production rate, m_α''', required for solving the mass conservation equation **(36)** is determined by the combustion model. The combustion model in FDS uses the Eddy Dissipation Concept (EDC), which assumes infinitely fast chemistry for non-premixed combustion such as pool fire.[57] [35]

Based on the above lumped species approach, 9.52 moles of Air react with 1 mole of Fuel and produce 10.52 moles of Products. Mass fraction of lumped species is denoted as Z_i, with N_Z tracked species. The background lumped species (Air) with mass fraction Z_0 is found by simple balance, $Z_0 = 1 - \sum_{i=1}^{N_Z} Z_i$. Two transport equations for lumped species Fuel and Product will be solved in this case.

Yield, mass produced per unit mass of fuel burned, of Carbon monoxide (CO) and soot in case on incomplete combustion needs to be defined by the user. [40]

The chemical source term for Fuel is modeled using EDC which is given as

$$\dot{m}_F''' = -\frac{\rho \min\left(Z_F, \frac{Z_A}{s}\right)}{\tau_{mix}} \tag{37}$$

Where *s* is the mass stoichiometric coefficient of Air and τ_{mix} is the time scale of mixing which is modeled depending on the filter width, Δ. The locally fastest process among diffusion, sub-grid scale advection and buoyant acceleration is considered as the time scale controlling process.

The mixing time scale can be mathematically expressed as,[36]

$$\tau_{mix} = \max\left(\tau_{chem}, min\left(\tau_d, \tau_u, \tau_g, \tau_{flame}\right)\right) \tag{38}$$

$$\tau_d = \frac{\Delta^2}{D_F} \tag{39}$$

$$\tau_u = \frac{\Delta}{\sqrt{2k_{sgs}}} \tag{40}$$

$$\tau_g = \sqrt{\frac{2\Delta}{g}} \tag{41}$$

where τ_d is the diffusion time scale which characterizes the DNS solution when the grid size is smaller than the Kolmogorov scale, $\eta . \tau_u$ is the time scale at higher Reynolds number dominated by turbulent convection transport. τ_g is the time scale where mixing time is controlled by buoyancy. τ_{flame} denote the upper limit of time scale and suggests that all the reaction shall take place before the flame extinction. D_F, is the diffusivity of the fuel and k_{sgs} is the sub-grid scale kinetic energy modeled as per either Deardorff or Smagorinsky turbulence model.

The heat release rate per unit volume is found as a product of the heats of formation of species and respective mass production rate.

$$\dot{q}''' = -\sum_{\alpha} \dot{m}_{\alpha}''' \, \Delta h_{f,\alpha}^{0} \tag{42}$$

4.2 Burner size

Cell size *Δx* is related to the characteristic diameter, *D**, of the fire, which is proportional to characteristic heat release rate, $Q*$.[40]

$$D^{*} = (Q^{*})^{\frac{2}{5}} D = 1.55 \text{ m} \tag{43}$$

$$\mathrm{Q}^{*} = \frac{\dot{\mathrm{Q}}}{\rho_{\infty} \mathrm{C_p} \, \mathrm{T}_{\infty} \sqrt{\mathrm{g}} \mathrm{D}^{\frac{5}{2}}} = 2.25 \tag{44}$$

where $\dot{Q}$ is the Heat Release Rate (HRR) of the fire. The theoretical heat release rate of the fire can be found by using the mass burning flux and the burning surface area.

$$\dot{Q} = \dot{m}'' A_p \Delta H_c = 3.23 \text{ MW} \tag{45}$$

The ratio *($D^*/\Delta x$)* is number of computational cells across the characteristic fire diameter.[40] The more the number of cells across the characteristic fire diameter, better the resolution of turbulence and small scale eddies, approaching DNS at high numbers.

The cell size, Δx,, was varied and cell size of 10 cm, 5 cm, 4 cm, 3 cm and 2.5 cm were studied whilst the ratio, D^*/dx, were 15, 30, 40, 50 and 60 respectively.

4.3 Source term

The mass burning flux obtained from differential pressure transducer in the experiment was used as the source term of the fuel (methane) in the simulations. The mass burning flux for small scale experiment under consideration described was 0.06446 kg/(m^2.s).[21] The orange area in Figure 5 represents the burning surface.

4.4 Boundary conditions

The “OPEN” boundary condition in FDS applied on the sides and the top of the fire to simulate atmospheric conditions. The domain of simulation was decided based on the coarse grid simulation. The domain was increased so that no visible eddies were observed on the edges of the domain. The domain selected for mesh sensitivity study was 2m x 2m x 6m. This domain is called as “fire mesh” for further references.

Once the mesh independent study was performed, the domain was scaled to a larger domain so as to facilitate inclusion of wind. The same domain of the size of “fire mesh” for analyzing wind effect result in undesirable effect due to complex interaction between the “OPEN” boundary condition. The “OPEN” boundary condition in FDS indicate atmospheric pressure condition outside the geometry to which it is applied.[40]

Figure 6 below illustrates the effect of domain on the velocity contour in a 3m x 3m plane at 1m above the floor surface. The wind of velocity 0.5m/s flows in the domain from the left side of the graph.

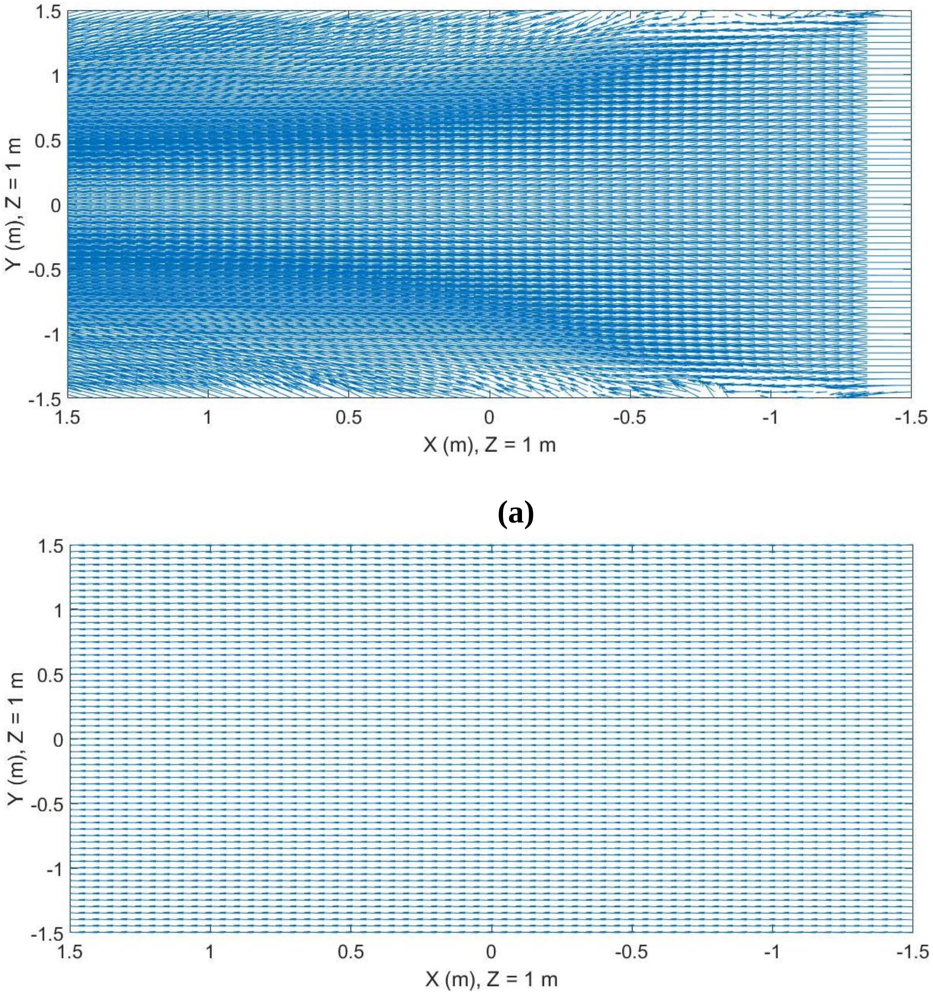

(a)

(b)

Figure 6: Effect of domain on velocity.
(a) Small domain (b) Wider domain

Figure 6 (a) shows velocity contour when the wind boundary condition is applied to the same "fire mesh". The "OPEN" boundary condition on the remaining three sides of the domain result in complex velocity contour which does not setup a desired velocity field. Figure 6 (b) shows the velocity contour in the "fire mesh" when the domain is stretched and wind boundary condition is applied on the boundary of the new domain. The dimensions of the domain in this case are 5m x 5m x 6m.

4.5 Time for simulation

Puffing frequency of the fire is used to determine the time for simulation. Equation (13) is used for preliminary estimation of puffing frequency. For the small scale experiment, the puffing frequency using equation (13) is

$$f = \frac{1.68}{\sqrt{1.12}} = 1.58\,Hz \tag{46}$$

The expected time period for oscillation is 0.61 sec. The duration of simulation was decided to be 30 times the time period of oscillation. This was based on the observation that it takes approximately 5 seconds for the transient ire to reach a steady oscillation state. So, 30 cycles of oscillations were simulated to ensure steady state fluctuations of desired parameters.

5 RESULTS AND DISCUSSION

The methodology discussed in previous section is applied to the experiment discussed in Section 3.

5.1 Mesh sensitivity study

Mesh size used for mesh sensitivity study are shown in the Table 4. The dimensions of the computational domain were 2m x 2m x 6m. The mesh sensitivity analysis was performed for no wind conditions.

Last 15 steady cycles of fluctuations were used for time averaging of quantities such as temperature and the vertical (W) velocity.

Table 4: Mesh sizes for mesh sensitivity analysis.

dx (cm)	D*/dx	Number of cells
10	15	24,000
5	30	192,000
4	40	312,500
3	50	832,320
2.5	60	1,536,000

Figure 7 shows temperature variation along the Y axis of the fire at 50cm above the base of fire. A similar profile is expected for the temperature variation along the X axis of the fire due to symmetry and absence of wind. As the mesh size is reduced and smaller eddies are resolved, the underlying physics are better resolved.

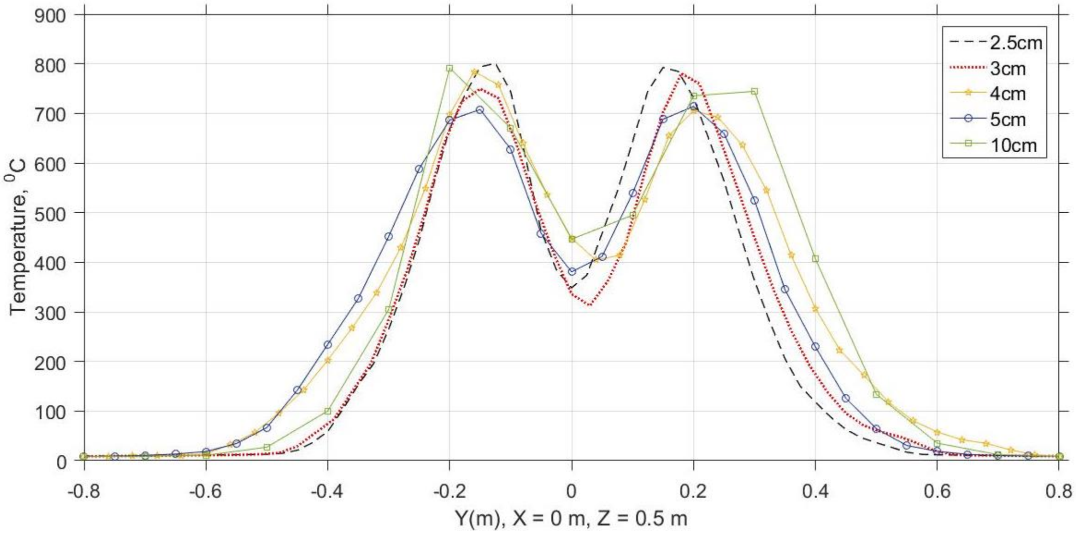

Figure 7: Temperature variation along Y axis at 50cm above the fire.

An interesting observation from the above figure is that lower the mesh size, less the temperature profile is affected. This could be due to the EDC for modeling mass production rate at small scale and the flame extinction methodology used in FDS. Combustion in FDS is suppressed if the potential heat release from combustion is not capable to raise the temperature of the reactant mixture above the critical flame temperature.[36] For a small mesh size, the combustion at the edge of the burner might not be sufficient to raise the temperature locally as high as compared to higher mesh sizes, which have more fuel and air in one cell and spans larger area of the burning surface. Lower the entrainment, lower will be the combustion of methane in the fuel rich zone of the fire, and thus, lower the temperature of the flame. However, since the temperature profile for 2.5 cm and 3 cm mesh are very close, it appears that the entrainment of air reaches a steady point.

Oxygen mass fraction and methane mass fraction variation with mesh size was observed along the height, Z, at X = 0 m and Y = 0 m. The existence of unburnt fuel at lower elevations is observed for lower mesh sizes.

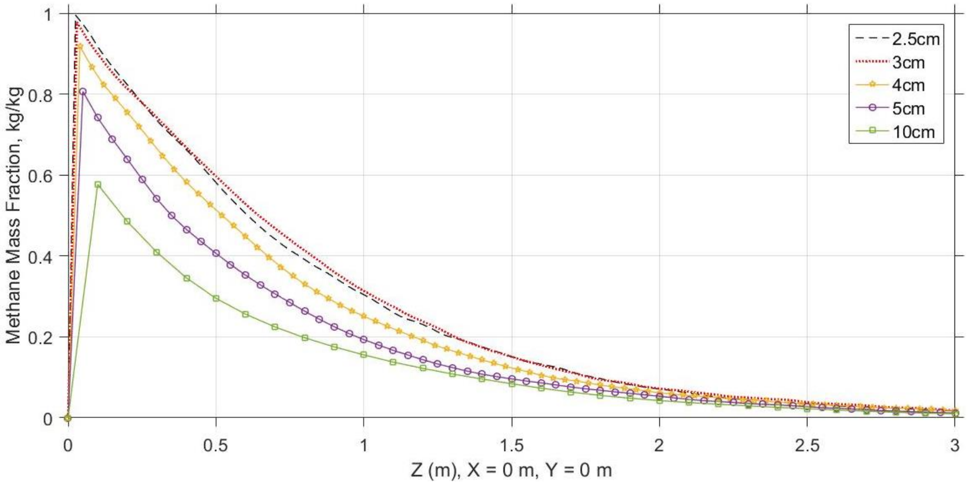

Figure 8: Methane mass fraction vs height for different mesh sizes.

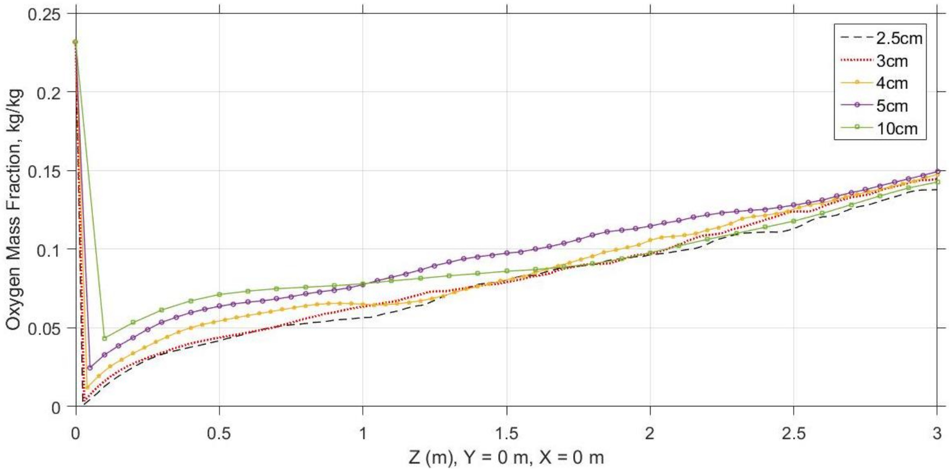

Figure 9: Oxygen mass fraction vs height for different mesh sizes.

In Figure 8 and Figure 9, the mass fraction at Z = 0 m is zero or equivalent to initial ambient values because of their location on the boundary cell, where the default FDS value is that of the initial surrounding environment. This is not a computation error.

The mass fraction of each species is obtained from the solution of conservation of mass for the lumped species. The Sub Grid Scale (SGS) kinetic turbulence energy (m^2/s^2) change with mesh size since eddies smaller than the filter width (mesh size) are modeled using the turbulence models. The SGS turbulence kinetic energy is computed from the turbulent viscosity modeled by using the Deardorff model, as discussed in section 4.1.1.

The mixing time scales for diffusion, convection and buoyancy for elevation of 50 cm is calculated, as explained in section 4.1.2, using the equations (39), (40) and (41) respectively. Variation of sub-grid kinetic energy and mixing time scales with the mesh size is shown in Table 5 for this specific point, Y = 0 m, X = 0 m, Z = 50 cm.

Table 5: SGS kinetic turbulence energy vs mesh size.

	2.5cm	3cm	4cm	5cm	10cm
κ_{sgs}, Z = 50cm (m^2/s^2)	0.054	0.048	0.075	0.107	0.18
κ_{sgs}, Z = 100cm (m^2/s^2)	0.169	0.177	0.195	0.352	0.377
τ_d (sec)	3.7	5.3	9.4	14.7	58.8
$\tau_u, Z = 50\ cm$ (sec)	0.076	0.097	0.103	0.108	0.167
$\tau_u, Z = 100\ cm$ (sec)	0.043	0.05	0.064	0.06	0.115
τ_g (sec)	0.07	0.078	0.09	0.1	0.14

As seen from the above table, the local mixing controlling time scale at Z = 50 cm for the reaction is buoyancy time scale, τ_g (sec). Thus, the mixing time scale, which directly contributes to the mass production rate via EDC, as given by equation (37), decreases with decrease in mesh size. All the oxygen is consumed by the time the air can reach the center of the fire at this elevation. Thus, the oxygen mass fraction and methane mass fraction are directly affected by the mesh size.

Above analysis of mixing time scale and effect on temperature profile indicate lower entrainment rate with decrease in the mesh size. Average horizontal velocity determined at Z = 30 cm for the above mesh sizes studied is shown below in Figure 10.

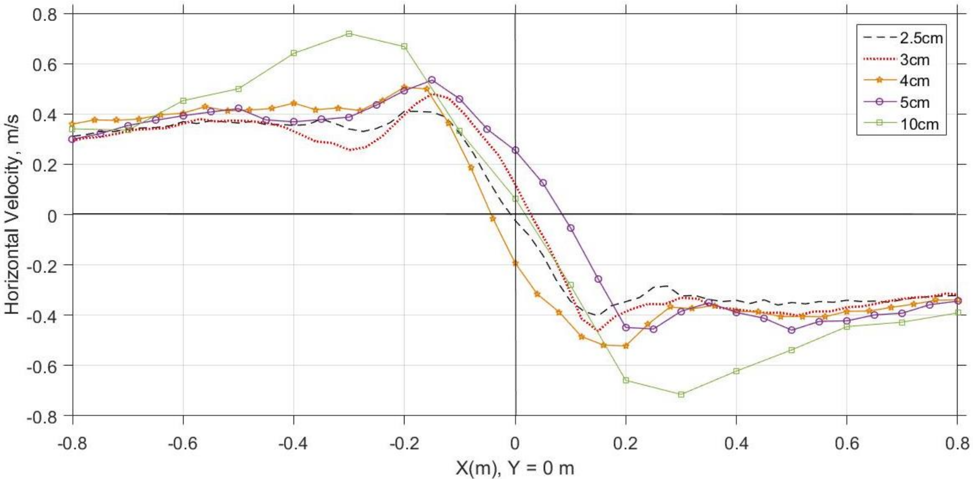

Figure 10: Average U – Velocity along X (m), Y = 0 m.

The entrainment rate decreases with the mesh size, approaching 0 m/s at the X = 0 m, Y = 0 m for finer mesh size of 2.5 cm and 3 cm. This is reasonable and depicts mechanism of entrainment that happen in real fire scenario. Resolution of smaller eddies, thus, seem to capture the entrainment phenomenon with more precision.

RMS value of W-Velocity along with the mean of last 10 sec of simulation for three different meshes at Z = 50 cm is shown below in Figure 11. RMS value is shown with the help of the error bars to observe the turbulent characteristics of the flow at each location for different meshes. The root mean square velocity of the W-velocity at Z = 50 cm and Z = 100 cm at X = 0 m and Y = 0 m is shown below in Table 6 for different mesh sizes.

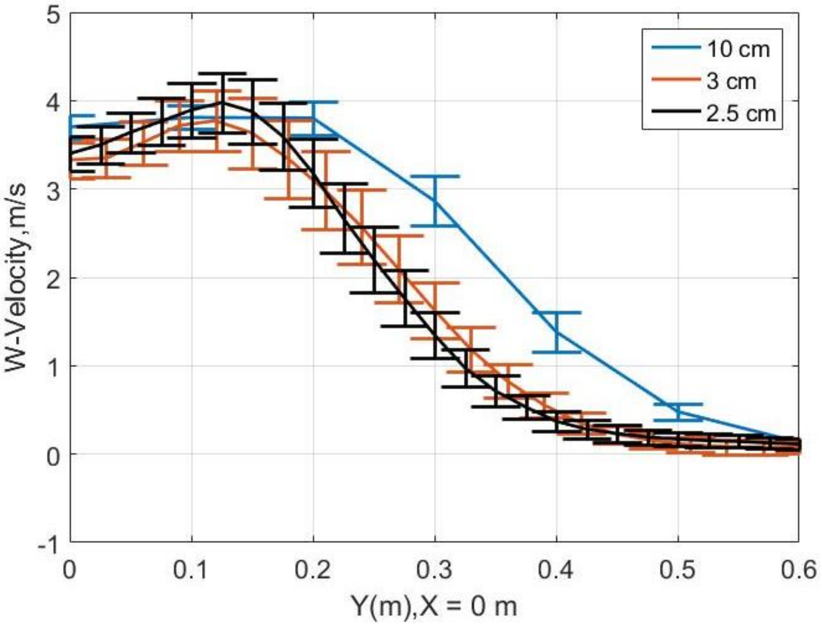

Figure 11: Vertical velocity with RMS value.

As the mesh size is reduced, more turbulence is resolved directly and less turbulent scales need to be modeled using the turbulence model.

Table 6: Root mean square velocity vs mesh size.

	2.5cm	3cm	10cm
W-Velocity, Z = 50 cm (m/s) (w)	3.59	3.25	4.36
RMS W-Velocity, Z = 50 cm (w_{rms})	0.892	0.835	0.691

	2.5cm	**3cm**	**10cm**
Turbulence intensity ($w_{rms}/\overline{w}$)	0.248	0.256	0.158
W-Velocity, Z = 100 cm (m/s) (w)	5.99	5.70	6.84
RMS W-Velocity, Z = 100 cm (w_{rms})	1.923	1.801	1.242
Turbulence intensity ($w_{rms}/\overline{w}$)	0.321	0.316	0.182

The RMS velocity is evaluated using the following formula,

$$u_{rms} = \sqrt{\frac{\sum_{i=1}^{n}(u_i - u_{mean})^2}{n-1}} \qquad \textbf{(47)}$$

The RMS value is an indication of turbulent fluctuation. Thus, smaller the mesh size, the turbulent fluctuation i.e. standard deviation is higher due to better resolution of smaller scales than by using coarser mesh size.

5.2 Pool fire structure

A fuel rich zone at the bottom of the fire which constitutes unburnt fuel due to unavailability of enough oxygen for complete combustion can be observed in FDS for smaller mesh sizes. The fuel rich zone forms the base of the fire structure in the three zone representation of the fire. The pool fire structure described by the three zone representation can be studied with the help of FDS.

Vertical velocity variation along the y-axis is evaluated at 11 different heights above the base of the fire. The extent of y-axis that spans the burning surface is from Y = -0.5 m to Y = 0.5 m. Figure 12 shows the variation of W-Velocity at each of these elevations along the burning surface at X = 0 m. The W-Velocity is averaged for the last 10 sec of the simulation time. Some interesting observations can be made based on the figure.

First, the fuel rich zone of the fire which is fixed to the base of the fire is observed until the height between Z = 80 cm and Z = 100 cm where the w-velocity at the center is maximum indicating combustion due to sufficient mixing with air. The W-velocity at the edge indicate separation from the base, thus a possible start of the second zone of pool fire.

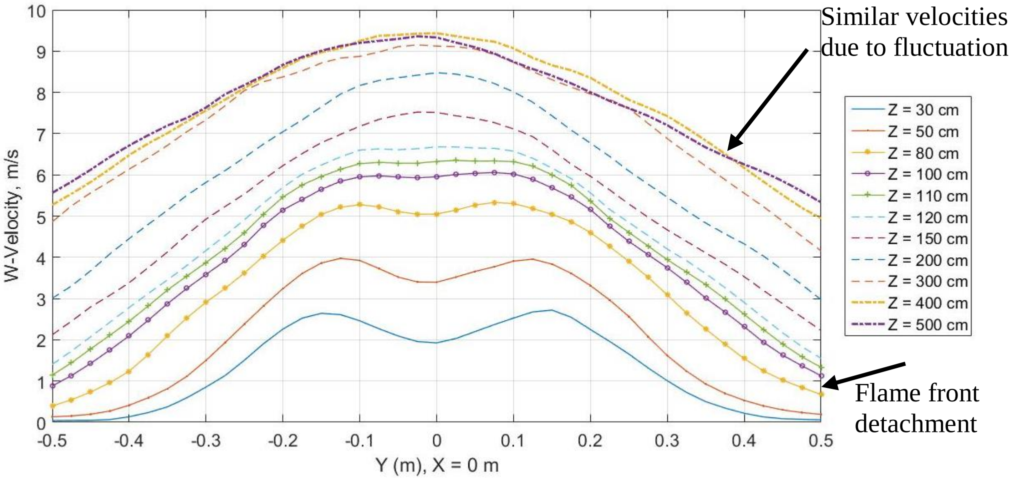

Similar velocities due to fluctuation

Flame front detachment

Figure 12: Vertical velocity describing pool fire structure.

The vertical velocity profile at Z = 400 cm and Z = 500 cm along the y – axis of the fire is almost the same which could be due to completion of combustion approximately between these elevation. Thus, a visible flame height can be expected to lie somewhere around this elevation.

Temperature profile for flame is shown below in Figure 13 resembles a better insight into the pool fire structure. Necking phenomenon due to air entrainment near the base of the fire can be clearly seen to exist around 0.5 m elevation. The fuel rich zone is observed to be anchored to the base until around 0.8 m elevation.

Once the flame separates from the fire and combustion takes place, random puffs separate from the fire. The zone 2 stretches from around 0.8 m until 2.5 m where the temperature is maximum and then starts falling, indicating less combustion due to puff separation.

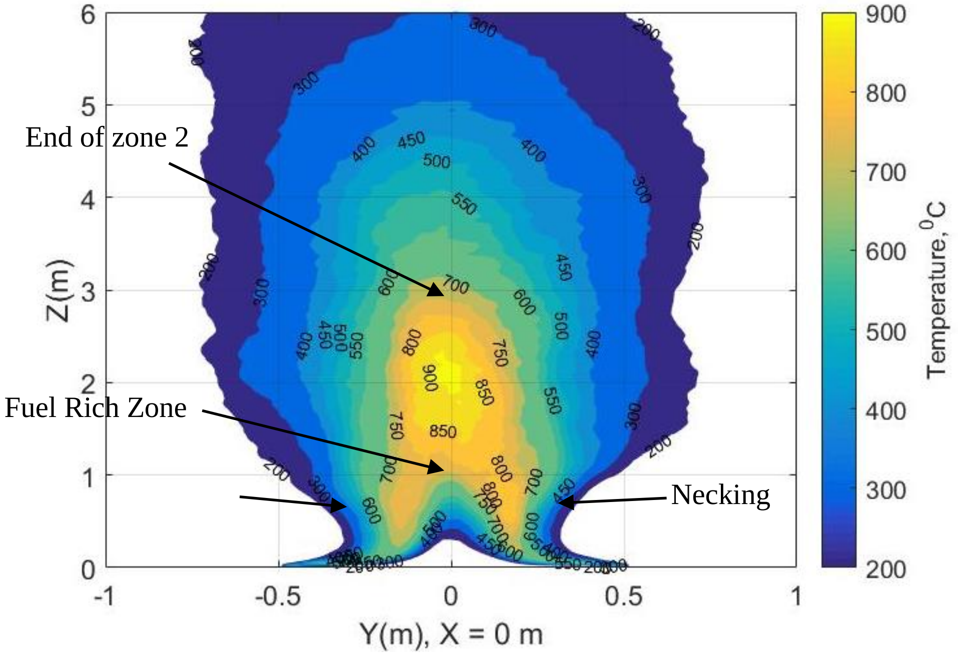

Figure 13 : Temperature describing pool fire structure.

Above analysis illustrates how results from CFD be used to describe the flame structure. However, the pulsation of the fire was not studied in depth during the above analysis. Since the pulsation of the fire is governed by a transient phenomenon, a more in depth study is performed for evaluating the oscillatory movement of fire.

5.3 Pulsation frequency

Lower the mesh size, the less turbulence needs to be modeled using the turbulence models, as shown in Table 5 and Table 6. Thus, the oscillation frequency of the fire simulated in FDS was computed using the 2.5 cm mesh for accuracy. Observing the transient variation of vertical velocity at height 50 cm above the base of the fire at X = 0 m and Y = 0 m it is seen that, as the simulation proceeds in time, the velocity fluctuations reach a steady region where it fluctuates about its mean steadily.

Figure 14 shows the transient behavior of W-velocity superimposed on w-velocity field recorded by Tieszen et al.[54] at same location above the base of the 1m diameter fire, obtained by using PIV technique recorded every 5 ms. Transient state in FDS reaches steady state fluctuating state in around 5 seconds (around 10 time puffing time period), after which the oscillations are very close to the experimentally measured value.

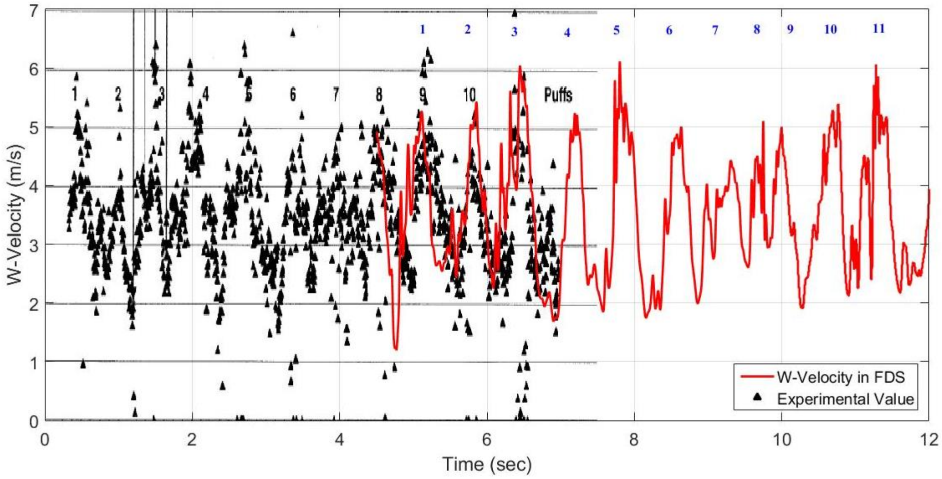

Figure 14: Transient W-Velocity behavior. Reprinted with permission from 54.

The experimental puffing frequency computed was 1.64 Hz using the W-velocity profile. Constant oscillations in FDS about 3.5 m/s indicate the pulsating nature of the fire and the ability of FDS to capture these oscillations. Visual inspection of the above graph indicate approximately 11 puffs over the period of 7 seconds. Thus, the expected frequency of oscillation is 1.57 Hz, or the puffing time period of 0.64 sec.

$$f = \frac{n}{t} = \frac{11}{7} = 1.57\ Hz \qquad (48)$$

where n is number of oscillation cycle observed and t is the time over which n oscillation are observed.

The four points, A, B, C and D shown in the Figure 15 are chosen to describe one cycle of oscillation of the fire. The velocity contours for these four points are shown in below in Figure 16.

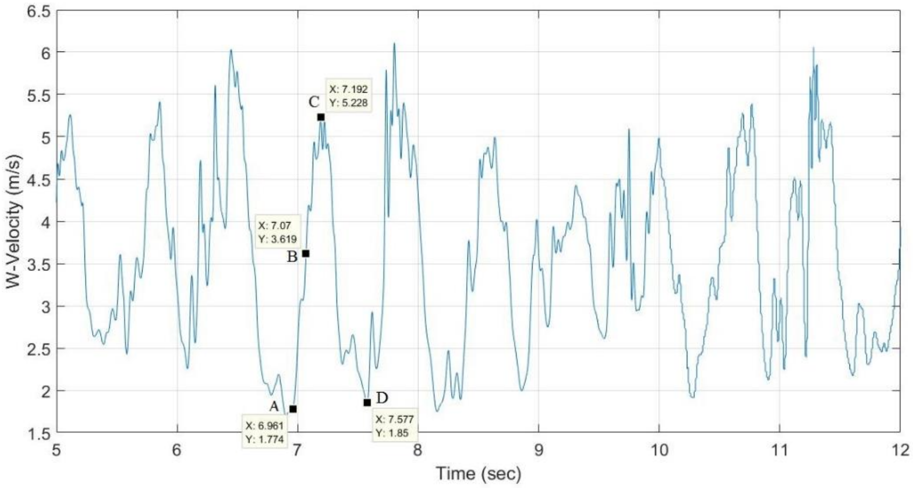

Figure 15: Instantaneous W-Velocity from 5 to 12 sec.

Figure 16 (a) shows the velocity contour at 6.96 sec, which is at the start of the oscillation cycle. The toroidal vortices at the edges can be seen at this instance due to which air entrainment begins.

Figure 16 (b) shows the velocity contour at 7.07 sec, which is quarter time period into the oscillation cycle. The velocity increases in the w-direction at this time and the fire plume starts rising at this point. The flame expands due to combustion at around Z = 0.8 m.

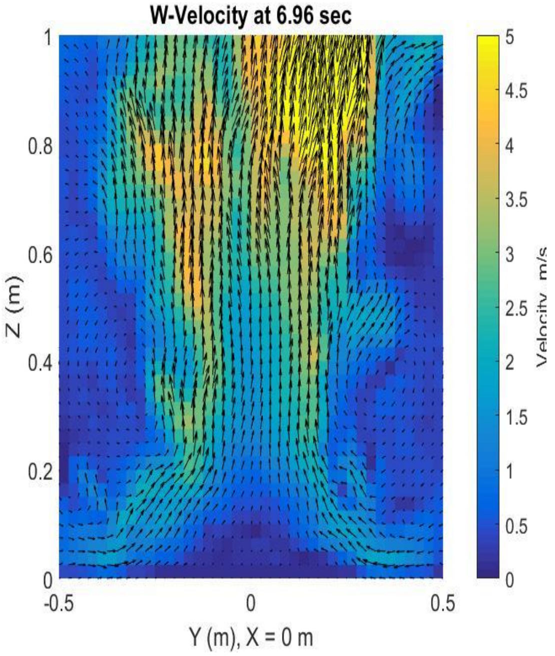

(A)

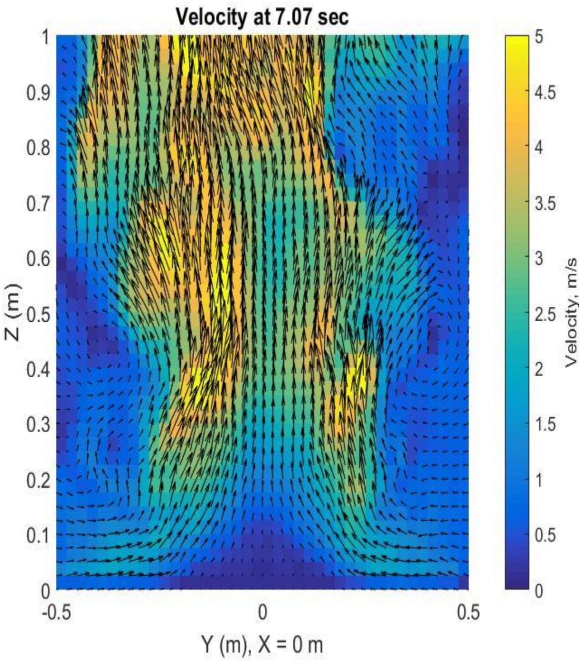

(B)

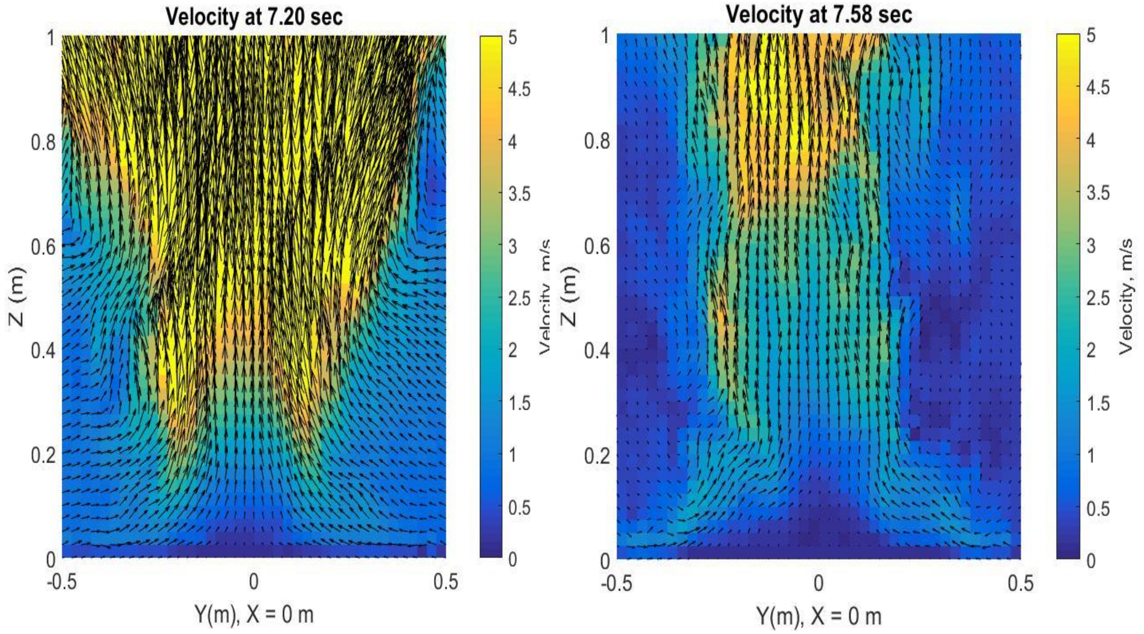

(C) (D)

Figure 16: Instantaneous velocity contour of one oscillation cycle.

(A) Velocity at 6.96 sec. (B) Velocity at 7.07 sec (C) Velocity at 7.20 sec. (D) Velocity at 7.58 sec

Figure 16 (c) shows velocity contour at 7.20 sec, which is at the peak of the cycle. At this instance, more fuel is in contact with the air and combustion causes the plume to rise due to buoyancy. W-velocity is the highest at this point of time.

The cycle completes at 7.58 sec shown in Figure 16 (d) where the fire return back to its original state. The fuel rich zone is observed to be anchored to the base until an elevation of around 80 to 100 cm where the w-velocity remains fairly low as compared to the surrounding region.

Power spectrum of instantaneous vertical velocity was obtained to study the oscillation frequency. A Fast Fourier Transform (FFT) algorithm was used to analyze 8192 samples from FDS for 8.5 seconds to obtain the power spectrum of the frequency.

The Maximum Entropy Method was applied to the 10 sec data having 9622 samples from FDS. The highest resolvable frequency in both the cases is 480 Hz. The experimental data sampled at a frequency of 1 Hz was recorded for around 880 seconds of the free burning period. Thus, the highest resolvable frequency from the experimental data is only 0.5 Hz. Since high frequency cannot be resolved from the experimental data, the puffing frequency obtained here cannot be compared with frequency obtained from the experimental data of this experiment.

The power spectrum obtained by using FFT is shown in the Figure 17, which identifies maximum peak at 1.53 Hz. However, two smaller peaks are observed. The FFT is not able to resolve the data effectively, maybe due to the noise in the data.

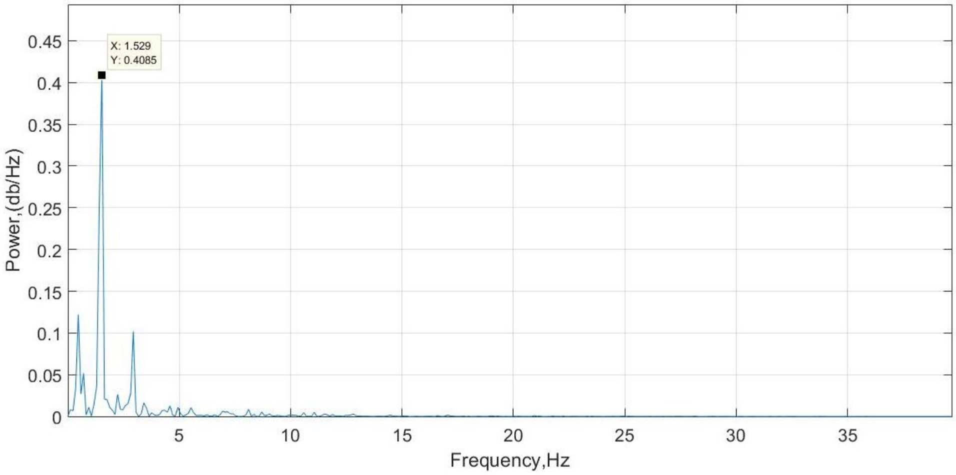

Figure 17: Power spectrum of W-Velocity using FFT.

For better accuracy and to see if the other two peaks resemble any physical aspect of the fire, Burg’s method of Maximum Entropy Method (MEM) is applied. The power used for Burg’s method is 3000. Higher order for Burg’s method does not show any other dominant peak in the power spectrum. Lower power does not give a clear peak and higher power result in the peak at similar frequency.

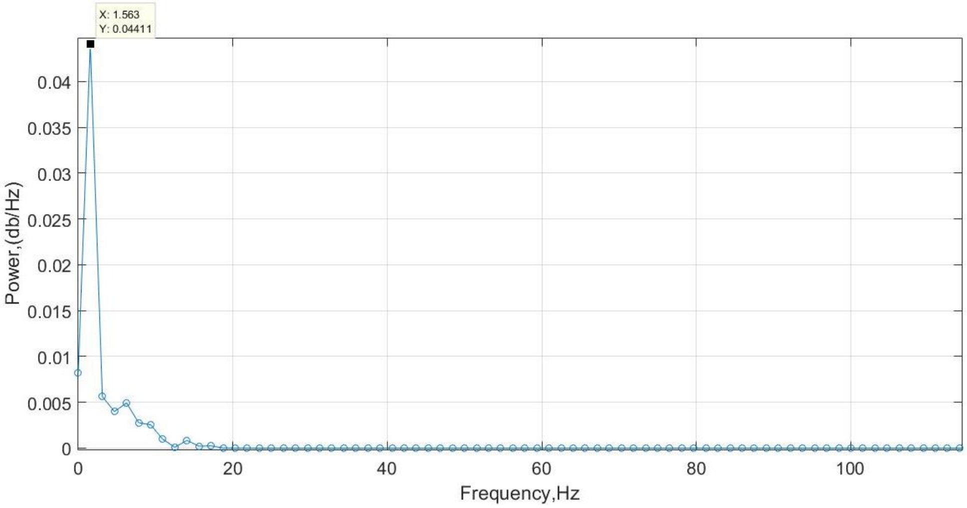

Figure 18: Power spectrum using MEM.

The puffing frequency of the small scale fire obtained from FDS is 1.56 Hz. The time period of oscillation is 0.64 seconds. This frequency is in agreement with experimental value of 1.65 Hz by Tieszen et al.[54] The oscillation frequency predicted is close to frequency computed by using empirical correlation developed by Malalsekara et al.[31] , which is 1.58 Hz, as discussed in Section 4.5. Thus, the LES methodology in FDS resolves temporal fluctuation of fire to great accuracy.

5.4 Simulation of the experiment

A thorough mesh sensitivity study performed earlier leads to the conclusion that the 3 cm mesh is sufficient to study the fire dynamics of the experiment studied here at affordable computational expense.

Two turbulence models, Deardorff model and Smagorinsky model are studied during further analysis. The wind condition in the experiment is included in FDS with the help of velocity boundary condition in negative X direction. For doing so, the domain is increased to avoid complex velocity profile in the region of "fire" due to interaction with "OPEN" boundary condition. This phenomenon is illustrated earlier in Section 4.4. The resulting domain size was 9.6 m x 9.6 m x 6 m with uniform grid starting from fine mesh of 3 cm in the region of the fire spanning 2.4 m x 2.4 m x 6 m, coarse mesh of 12cm around it within 4.8 m x 4.8 m x 6m, and the coarser mesh size of 0.24 cm in the rest of the domain.

A visual comparison fire at a certain time instance simulated by FDS and snapshot from experiment is shown below in Figure 19.

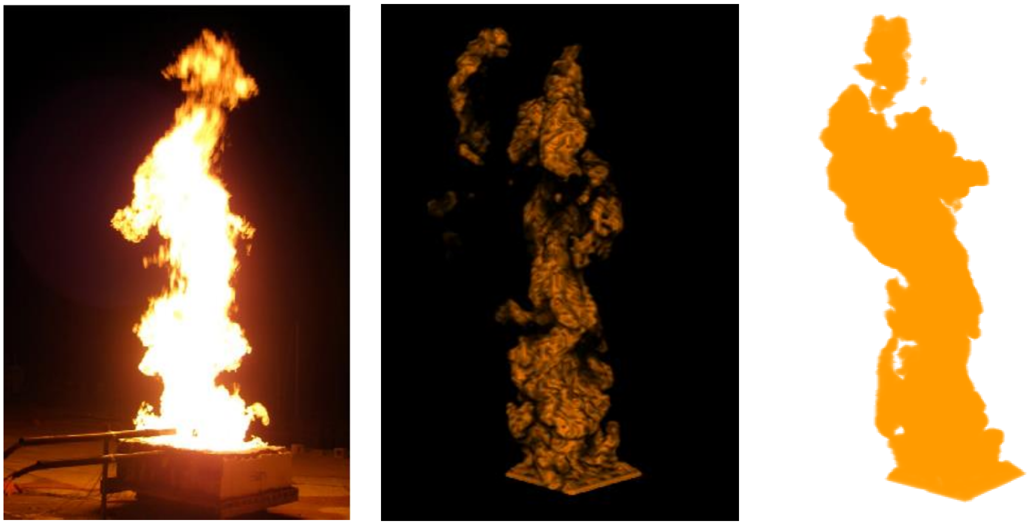

(a) (b) (c)

Figure 19: Visual comparison of experiment and the simulated fire.

The Figure 19 (a) is the snapshot of the experimental fire at some time instance. Figure 19 (b) is the fire displayed in SmokeView which is described by the iso-surface of HRRPUV more than 200 kW/m^3. A color map is used to describe the surfaces with

HRRPUV more than 200 kW/m^3, thus giving it a realistic display. Figure 19 (c) is a similar representation without the color map to describe higher HRRPUV surfaces.

5.4.1 Centerline temperature

Temperature at the centerline of the fire computed by FDS was compared with the temperature gauges at the centerline above the surface of the liquid pool. A steady burning phase of the real fire was observed after about 5 minutes of free burning. Thermocouple data during this steady burning phase was time averaged over 120 sec. An example of Normal Quantile plot of thermocouple 0.2032 m (8”) above the concrete surface is shown below in Figure 20. The mean is 402 ^{0}C with standard error of 3.87. The QQ-Plot shows near normal behavior of the data indicating steady state burning of the fire.

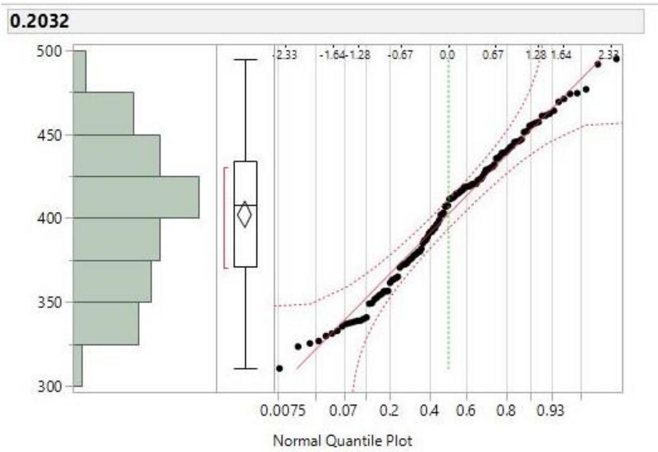

Figure 20: Example of normal quantile plot of thermocouple data.

The liquid level at the time this data was extracted was around 10 cm. Since FDS simulation in this study does not simulate evaporation of liquid but uses the mass burning flux prescribed by the user at the boundary of the pool, the liquid height was neglected during the comparison of flame temperature. The liquid level was assumed to be constant during this 120 sec time period of averaging.

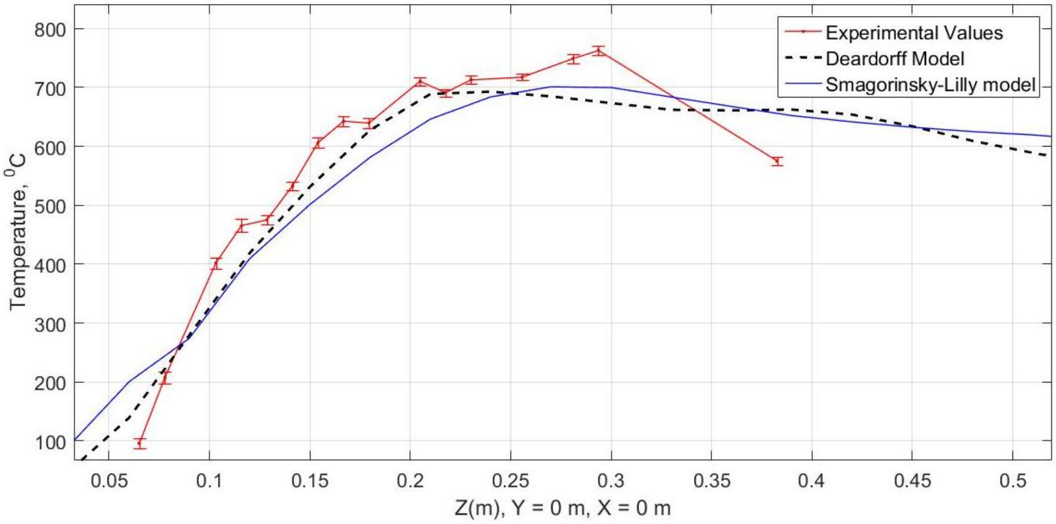

Figure 21: Flame temperature vs experimental data.

The Squared Error (SE) is evaluated using the following formula,

$$SE = \sum_{i=1}^{n} \left(T_{i,model} - T_{i,expt}\right)^2 \tag{49}$$

where $T_{i,model}$ is the temperature predicted when a specific turbulence model is used and $T_{i,expt}$ is the temperature measured by the thermocouple during the actual experiments.

The squared error for Deardorff model and Smagorinsky model using is estimated to be 5.5 x10^4 and 6 x 10^4 respectively. At elevations closer to the burning surface, both the models predict the temperature with similar squared error with respect to experimental data. This could be due to the mixing time scale in EDC model, which is limited by buoyant time scale and independent of modeled sub-grid kinetic energy until about 1m above the base of the fire at X = 0 m, Y =0 m. The magnitude of buoyant time scale which controls the combustion time scale at 50 cm and 100 cm elevation is shown in Table 5.

The turbulent convective transport time scale is inversely dependent on square root of sub-grid turbulent kinetic energy, thus the temperature is directly affected by the choice of turbulence model.

The modeled sub-grid kinetic energy shown below in Figure 22 show how the sub-grid turbulence energy modeled by Smagorinsky model is higher than Deardorff model at higher elevations.

Table 5 shows convection time scale limits the reaction time scale above approximately 0.17 m^2/s^2 of sub-grid kinetic energy. Thus, large differences observed downstream are owing to the change in combustion controlling time scale from buoyant to the turbulent convective transport time scale.

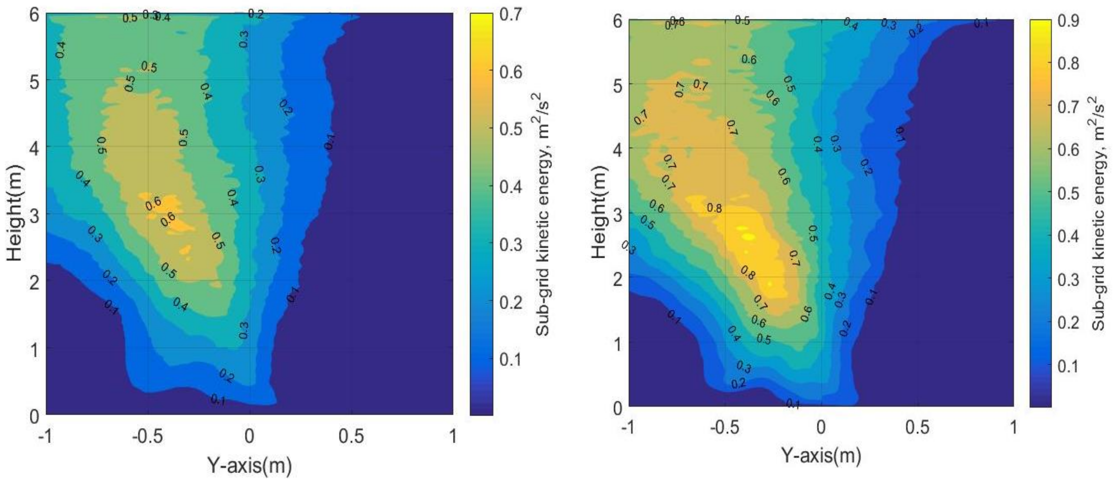

(a) (b)

Figure 22: Sub-grid kinetic energy for two turbulence models.

(a) Deardorff model and (b) Smagorinsky model

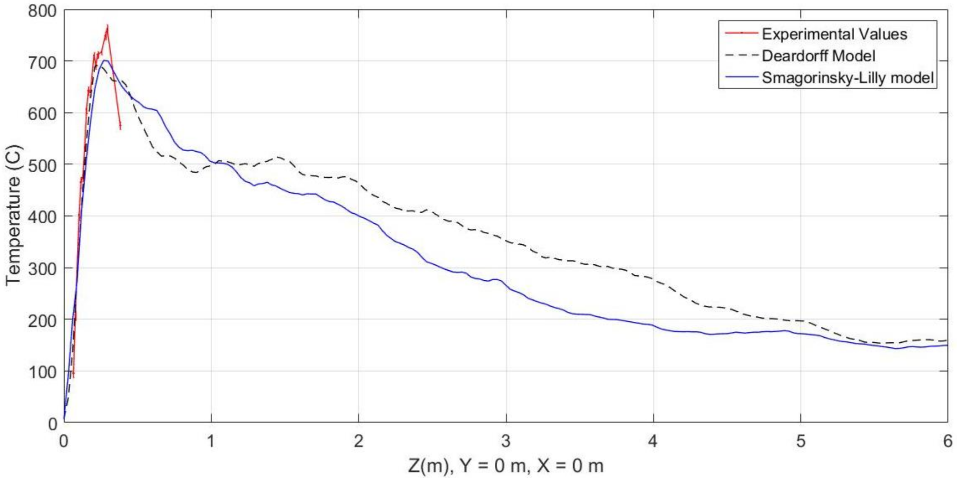

Figure 23: Flame temperature along Z axis, Y = 0 m, X = 0 m.

Since the thermocouple data may be affected by convection, radiation and conduction in the fire, the FDS predictions of temperature are very promising. However, temperature predictions further downstream cannot be compared to experiment due to lack of data. Assessing the effect of these models on the flame geometry could give an insight into a better of these two turbulence models.

5.4.2 Flame geometry

Flame length, height and tilt were studied to assess flame geometry. Two methods were utilized for determining the flame geometry using FDS. First involved use of Heat Release Rate Per Unit Volume (HRRPUV) to define the visible flame boundary and the second involved the use of temperature. The experimental value for the studied flame geometry is summarized below in Table 7. Flame geometry measured from the experiment was computed by processing images obtained from the high speed camera.

Table 7: Flame geometry determined from experiment[21].

	Tilt (degrees)	Length (m)	Height (m)
Mean	13.5	4.3	4
Standard Error	±7.3	±0.6	±0.6
Maximum (U_b)	20.8	4.9	4.6
Minimum (L_b)	6.2	3.7	3.4

Contour of time averaged HRRPUV on the Y plane at X = 0 m is evaluated when both turbulence models, Deardorff and the Smagorinsky model, were used. Figure 24 and Figure 25 represent HRRPUV contour for Deardorff and Smagorinsky model.

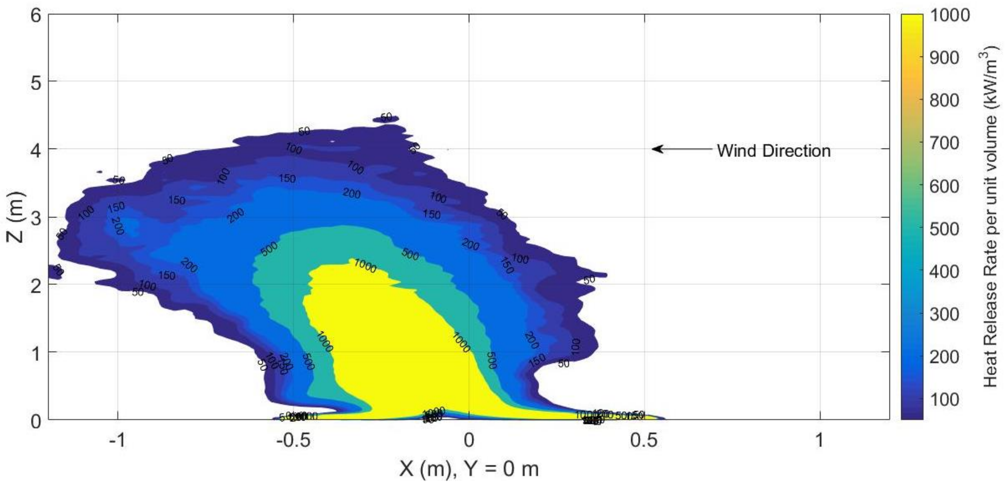

Figure 24: Average HRRPUV contour using Deardorff model.

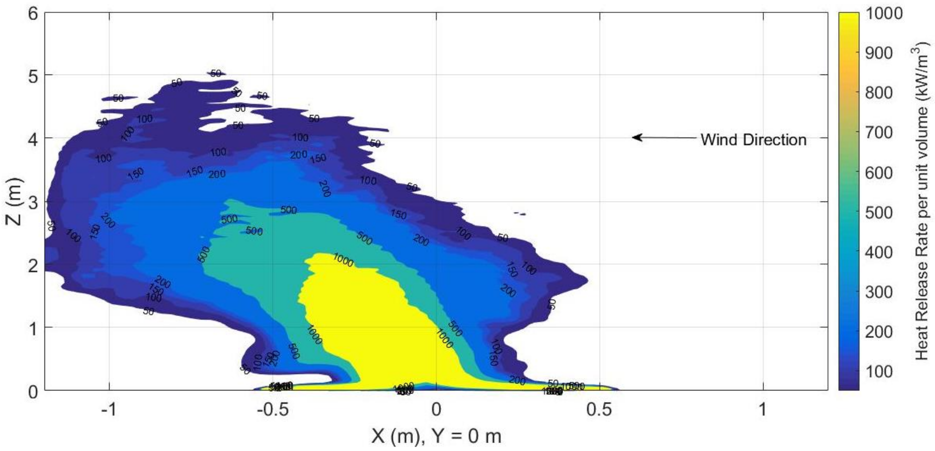

Figure 25: Average HRRPUV contour using Smagorinsky model.

Flame boundary was described by using the iso-surface of 50 kW/m^3 HRRPUV. This value was chosen after observing the instantaneous HRRPUV. Some instantaneous snapshot from FDS for one puffing cycle are shown below in Figure 26. Majority of the combustion is observed to be enclosed within this iso-surface of 52.9 kW/m^3. Thus, this HRRPUV value ensure the visible fire is enclosed within the iso-surface.

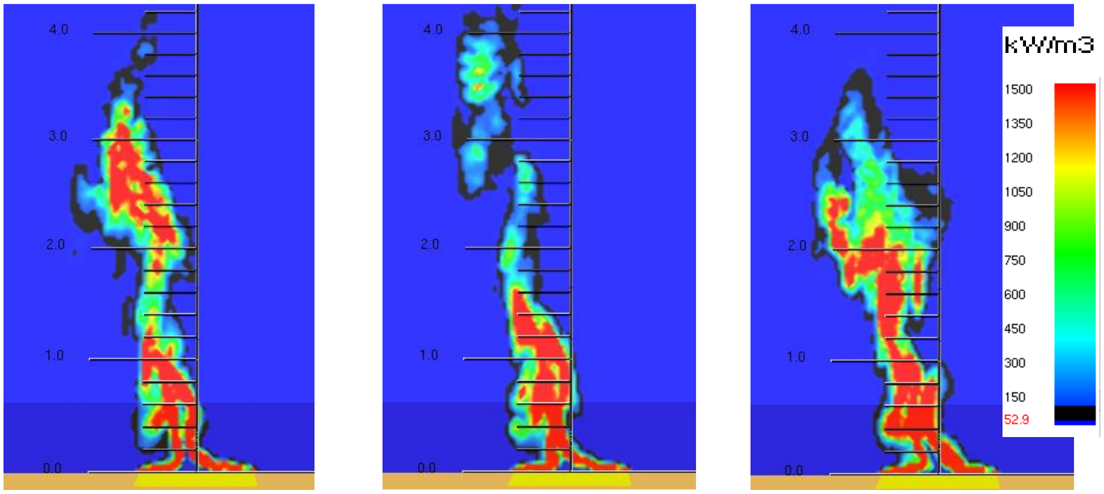

(a) 9.56 sec (b) 9.7 sec (c) 10.2 sec

Figure 26: Instantaneous HRRPUV in SmokeView.

A time averaged HRRPUV contour will not show any puffs since the time for averaging is 10 seconds. Each point on time averaged iso-surface of 50 kW/m^2 is traced and its distance from the center of the base of the fire is calculated. The point lying farthest from the center of the base is considered as the flame tip and its distance from origin as the flame length. The flame height is the corresponding y-coordinate. The flame tilt is the angle between the vertical line, X = 0 m, Y = 0 m, and the line joining the X = 0 m, Y = 0 m and the farthest point. The flame geometry assessed by using flame geometry enclosed by HRRPUV iso-surface of value 50kW/m^2 is summarized below in Table 8.

Table 8: Flame geometry using HRRPUV iso-surface of 50kW/m^3.

Turbulence model	**Deardorff**			**Smagorinsky**		
	Mean	Max error	Min error	Mean	Max error	Min error
Tilt(Deg)	9.1 (-32%)	11.72	2.88	11.8 (-13%)	9.03	5.57
Length of flame(m)	4.4 (+1.6%)	0.67	0.53	5.0 (16%)	1.27	0.27
Height(m)	4.1 (+1.25%)	0.65	0.55	4.5 (12%)	1.06	0.14

The maximum error and minimum error is computed by using the following formulae.

$$MAX_{error} = MAX\big(ABS(L_b - Y), ABS(U_b - Y)\big) \qquad \textbf{(50)}$$

$$MIN_{error} = MIN\big(ABS(L_b - Y), ABS(U_b - Y)\big) \qquad \textbf{(51)}$$

Where, L_b is the lower bound of experimental data, U_b is the upper bound of experimental data and Y is the predicted value using either model. Thus, closer the maximum and minimum error values to each other, the closer is the predicted value to the experimental mean.

The numbers in the brackets show errors with respect to the mean of experimental value as shown in Table 7. The Smagorinsky model over predict the length and height by 16% and 12% respectively as compared to the Deardorff model, which over predict the length and height by only 1.6% and 1.25% respectively. However, the flame tilt is under predicted 13% when Smagorinsky model is used as compared to the 32% under prediction when using Deardorff model. However, both the tilt predictions are within the experimental uncertainty.

Second method involved determining the flame shape by establishing a suitable temperature iso-surface will enclose the visible flame. Time averaged temperature contour on the Y plane at X = 0 m is shown in Figure 27 and Figure 28. Due to radiation, the surrounding atmosphere is heated and thus iso-surface of ambient temperature will not describe the flame geometry.

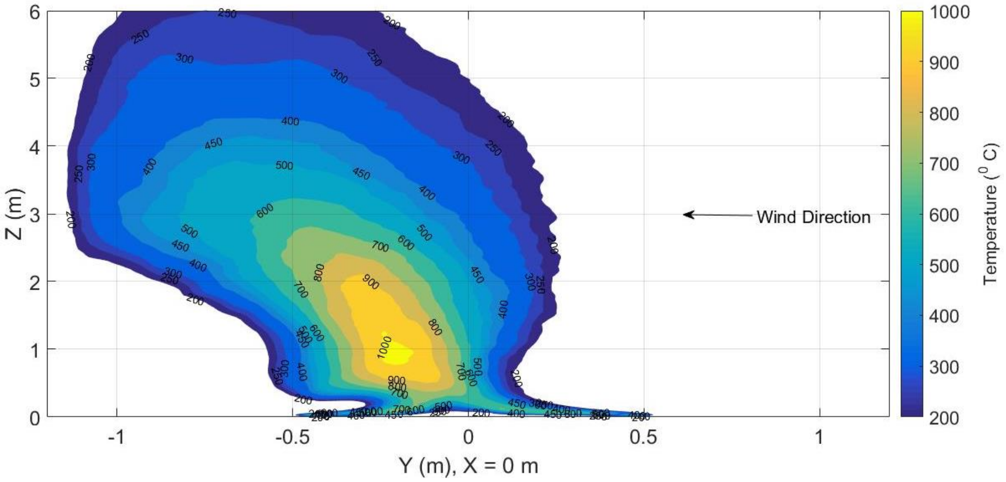

Figure 27: Temperature contour using Deardorff model.

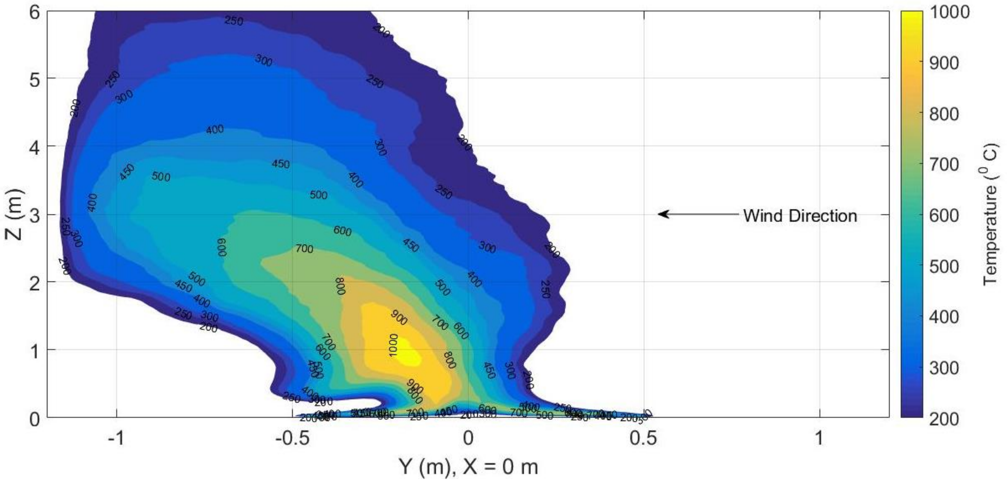

Figure 28: Temperature contour using Smagorinsky model.

For this reason, a sensitivity study was performed to determine adequate temperature so that it enclose the visible flame. Iso surface of 250˚C, 300˚C, 400˚C, 450˚C, 500˚C and 600˚C were used to predict the flame geometry and are compared with the experimental data to observe the variability. The flame length, tilt and height calculations are performed by using the same method by finding the point farthest from origin. The farthest point from the origin was considered to represent the flame tip and the tilt, length and height were computed accordingly.

Result of this sensitivity study obtained after using Deardorff model is shown in Figure 29. As the temperature of the surface defining the flame geometry is increased, the flame length and height decreases. This is expected as higher temperatures are observed closer to the base of the fire. At around 450˚C, the average flame length and height are close to the experimentally measured value. The values computed in this way is also close to the values computed by using the HRRPUV method. This validates that the flame geometry is described very well when the iso-surface describing the boundary of the flame has average temperature profile is 450˚C. Although infrared images for the experiment are not available, it will be interesting to study this phenomenon.

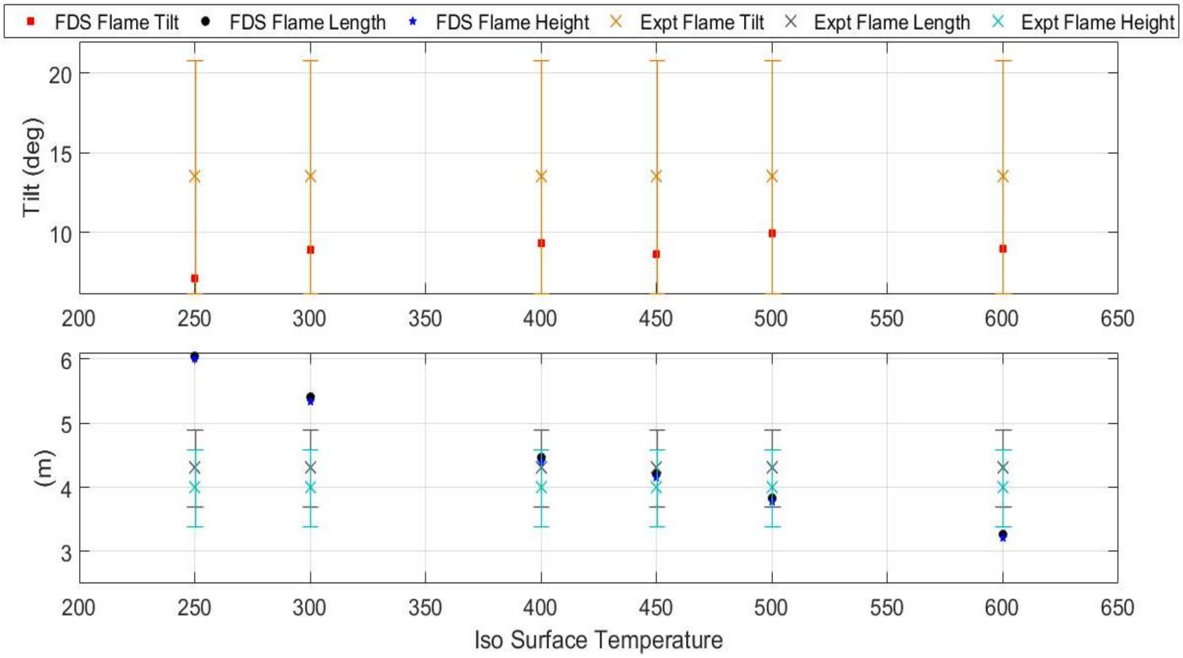

Figure 29: Flame tilt, length and height sensitivity with iso-surface temperature.

Iso-surface of 450˚C was used to determine the flame tilt, length and height using the Smagorinsky model. Once these desired flame geometry parameters were evaluated using FDS, empirical correlations described in Section 2.2 were used to determine the same parameters. The A.G.A correlation was used for determining flame tilt and the Thomas correlation for the Flame length. These empirical correlations are used in LNGFIREIII and thus were chosen to compare the accuracy.

Comparison of experimental data with FDS and empirical correlations is shown in Table 9.

Table 9: Flame geometry – Experiment vs FDS vs SFM.

Source	Tilt (degrees)	Length (m)	Height (m)
Experiment	13.5	4.3	4
Expt. Standard Error	±7.3	±0.6	±0.6
FDS-Deardorff model	8.6 (-36%)	4.2 (-2.4%)	4.2 (+3.8%)
FDS-Smagorinsky model	11.8 (-12%)	3.9 (-15%)	3.8 (-12%)
Empirical Correlations (used in LNGFIREIII)	0 (-100%)	3.72 (-13.5%)	3.72 (-7%)

The numbers in the brackets represent the error with respect to the mean of experimental value. The tilt of the flame predicted is zero since the A.G.A correlation assumes negligible tilt if the non-dimensional wind speed is less than 1. The flame length and height are thus the same for predictions from empirical correlations because of negligible tilt. The Deardorff model predicts the flame length and geometry within 3-4% of the experimental mean and Smagorinsky model predicts the same parameters within 12-15% of experimental mean.

5.4.3 Radiation from fire

Radiation from the fire is an important aspect for hazard analysis. Radiometer devices to monitor radiative flux from the fire were placed in the computational domain of FDS. The location was decided based on the four radiometers used in the experiments. Location of radiometers, R3 and R4, which were at a distance away from the fire. The location of R3 is X = -2m, Y = -2m, Z = 0.9 m and R4 is X = -2.2 m, Y = -0.1 m, Z = 0.9 m. The other two radiometers, R1 and R2, were placed at 11” and 19” above the base of the fire at Y = 0 m, X = 0 m. The primary purpose of these was to measure the radiative feedback from the fire. However, the reference temperature of the sensor in R1 and R2 changed over the duration of the test due to change in temperature of water used for maintaining the temperature.[21] Thus, the radiative fluxes measured by R1 and R2 are unreliable. All the four radiometers, have view angle of 150˚ and the radiative flux monitors used in FDS have view angle of 180˚. Thus, a higher prediction of the radiative flux from FDS is expected.

Solid Flame Model (SFM) was used for predicting the radiation at a distance for locations R3 and R4. The flame length obtained by using Thomas correlation, as shown in Table 9, was used to describe the cylindrical geometry of the flame. The transmissivity and view factor were computed by using the equations as described in Appendix A. Table 10 shows comparison of radiation obtained from different sources. The numbers in the brackets show the error with respect to the experimentally measured mean value

Table 10: Flame Radiation – Experiment vs FDS vs SFM.

Source	R1 (kW/m^2)	R2 (kW/m^2)	R3 (kW/m^2)	R4 (kW/m^2)
Experiment	32.6	24.6	2.5	5.0
Expt. Std. Error	±1.98	±1.05	±0.095	±0.19
FDS-Deardorff	33.8 (+3%)	31.5 (+28%)	3.1 (+22%)	5.5 (+11%)
FDS-Smagorinsky	38.8 (+19%)	36.2 (+47%)	3.5 (+39%)	6.4 (+28%
SFM	-	-	3.8 (+52%)	5.7 (+14%)

Deardorff model results in closer prediction of radiative flux away from the fire, 10-20% above experimental mean. On the other hand, Smagorinsky model result in higher prediction of radiation away from the fire, 30-40% above the experimental mean. The

SFM predicts radiation around 20-50% above the experimental mean. The Deardorff model result in prediction of the radiation closest to the experimentally measured values.

Radiative heat fraction of the fire is defined as overall radiative cooling rate, $\ddot{Q}_R$, divided by the product of mass burning rate *(kg/s)* and the ideal heat of combustion, ΔH_c *(kJ/kg)*.[55]

$$\chi_r = \frac{\ddot{Q}_R}{\dot{m}'' A_c \Delta H_c} \qquad \textbf{(52)}$$

The overall radiative cooling rate,$\ddot{Q}_R$, for Deardorff and Smagorinsky model were 0.369 MW and 0.414 MW respectively. Radiative fraction evaluated for Deardorff model was 11.4 % and the use of Smagorinsky model resulted in 12.8% of combustion heat to be radiated. The higher prediction of radiative fraction by using Smagorinsky model contribute to the higher radiative flux as compared to the Deardorff model.

The wide range of error while using SFM is attributed to the calculation of view factor. The view factor calculation assumes the location to be at a distance along the flame described by the cylindrical cross section in the direction of the wind. Radiation of interest should be calculated only at a distance downwind of the cylindrical cross section, unless the view factor is calculated in a way which considers 3D location of the point of interest.

6 CONCLUSIONS

This section lists a summary of important aspects studied during the analysis of simulation performed for a 1m x 1m LNG pool fire.

A. Comparative study of Deardorff and Constant coefficient Smagorinsky turbulence model shows sensitivity of flame characteristics on turbulence model.

  - The flame length and height predicted by using Deardorff model is about maximum 3.8 % above the experimental mean. On the other hand, Smagorinsky model leads to prediction of about maximum 16 % above the experimental mean.
  - The flame tilt is under predicted when either of the two turbulence models is used. Deardorff model under predicts by around 36% and the Smagorinsky model leads to under prediction of around 13%. However, both these predictions are within the experimental uncertainty.
  - The radiation at a distance from the fire is predicted the best with the use of Deardorff model, which predicts the radiation away from the fire about 15% above the experimental mean. The Smagorinsky model predicts about 25% above the experimental mean. The Solid Flame Model gives a wide range of variability with average 35% over experimental value.

B. Different numerical approaches were compared with the experimental values for determining the flame geometry of the fire. Physical shape of the flame of the fire under study can be described by an area enclosed by an iso-surface of 450˚C temperature. This flame shape can be used for determining flame geometry such as flame length, height and tilt.

C. The FDS captures the transient fluctuations of the fire with great accuracy and predicts the pulsation frequency close to the experimental measurements.

D. The pool fire structure can be studied in CFD by observing the vertical velocity and temperature profile.

6.1 Future work

This work was limited to validate FDS against small scale pool fire experiment and study sensitivity of pool fire on turbulence models. However, future extension of this work can be performed in few ways.

- Similar validation work can be performed for medium scale fire and the effect of soot formation on radiation should be studied.
- The three zone representation of the pool fire structure can be used to study average SEP variation with height for different diameters of fire using CFD. This could be used to refine/validate the model proposed by Raj[46], which considers SEP variation with height. This could lead to potential improvement of the empirical model.
- The radiation from the sun was neglected here since the experiments were performed during the evening in absence of any sunlight. However, radiation level may be higher in presence of solar radiation.

REFERENCES

1. A.G.A, *LNG Safety Program: Interim Report on Phase II Work,* 1974, Battelle Memorial Institute, Columbus Laboratories, American Gas Association.

2. Ansys, *12.0 ANSYS FLUENT Theory Guide,* Vol. 5, 2009: Ansys Inc.

3. Atallah, S. and Shah, J.N., *LNGFIRE - A Thermal Radiation Model for LNG Fires,* 1990, Gas Research Institute.

4. Babrauskas, V., *Estimating large pool fire burning rates,* Fire Technology, 1983, **19**(4): p. 251-261.

5. Baum, H.R., McGrattan, K.B., and Rehm, R.G., *Three dimensional simulations of fire plume dynamics,* Fire Safety Science, 1997, **5**: p. 511-522.

6. Becker, H. and Liang, D., *Visible length of vertical free turbulent diffusion flames,* Combustion and Flame, 1978, **32**: p. 115-137.

7. Becker, H. and Liang, D., *Total emission of soot and thermal radiation by free turbulent diffusion flames,* Combustion and Flame, 1982, **44**(1-3): p. 305-318.

8. Bilger, R., *Turbulent flows with nonpremixed reactants*, in *Turbulent reacting flows*,Turbulent reacting flows, 1980, Springer. p. 65-113.

9. Blanchat, T., Paul Helmick et al, *The Phoenix Series Large Scale LNG Pool Fire Experiments* 2011, Sandia National Laboratories.

10. Burgess, D. and Zabetakis, M., *Fire and explosion hazards of LNG,* US Bureau of Mines Investigation Report, 1962, **6099**.

11. CHIV, *Safety History of International LNG Operations,* 2002, CH.IV International,

12. Cooper, A., et al., *Macroeconomic impacts of increasing U.S LNG exports,* 2015, Leonardo Technologies, Inc.

13. Cox, G., Chitty, R., and Kumar, S., *Fire modelling and the King's Cross fire investigation,* Fire Safety Journal, 1989, **15**(1): p. 103-106.

14. CPD, *Methods for the calculation of the physical effects of the escape of dangerous material,* 2005, Committee for Prevention of Disasters,The Hague.

15. *Database of Hazardous Materials*, 2013, National Oceanic and Atmospheric Administration, https://cameochemicals.noaa.gov/, Accessed May 2016.

16. FERC, *Recommended Parameters for Solid Flame Models for Land Based Liquefied Natural Gas Spills*, 2013, Federal Energy Regulatory Commission,Washington, DC.

17. Foss, M.M., *Introduction to LNG : An overview on liquefied natural gas (LNG), its properties, the LNG industry, and safety considerations*, Research Consortium Publication, Commercial Frameworks for LNG in North America, 2012, The University of Texas at Austin.

18. GexCon, *FLACS v9. 1 User's Manual*, 2010: GexCon AS.

19. Greenshields, C.J., *OpenFOAM User Guide*, Vol. 3, 2015: OpenFOAM Foundation Ltd.

20. Hamins, A., Kashiwagi, T., and Buch, R.R., *Characteristics of pool fire burning*, in *Fire Resistance of Industrial Fluids*,Fire Resistance of Industrial Fluids, 1996, ASTM International.

21. Herrera Gomez, L.C., *Experiments for the Measurement of LNG Mass Burning Rates*, Master's Thesis, Texas A&M University, 2011.

22. Heskestad, G., *Luminous heights of turbulent diffusion flames*, Fire Safety Journal, 1983, **5**(2): p. 103-108.

23. Hightower, M., et al., *Guidance on risk analysis and safety implications of a large liquefied natural gas (LNG) spill over water*, 2004, Sandia National Laboratories.

24. Hostikka, S., Mcgrattan, K.B., and Hamins, A., *Numerical modeling of pool fires using LES and finite volume method for radiation*, Fire Safety Science, 2003, **7**: p. 383-394.

25. Ikealumba, W.C. and Wu, H., *Some recent advances in liquefied natural gas (LNG) production, spill, dispersion, and safety*, Energy & Fuels, 2014, **28**(6): p. 3556-3586.

26. Kelsey, A., Gant, S., and McNally, K., *Application of Global Sensitivity Analysis to FDS simulations to Large LNG fire plumes*, in *Hazards 24*. 2014, Crown.

27. Köylü, Ü.Ö. and Faeth, G.M., *Carbon monoxide and soot emissions from liquid-fueled buoyant turbulent diffusion flames*, Combustion and Flame, 1991, **87**(1): p. 61-76.

28. Launder, B.E. and Spalding, D., *The numerical computation of turbulent flows,* Computer methods in applied mechanics and engineering, 1974, **3**(2): p. 269-289.

29. *Liquefied Natural Gas Facilities: Federal Safety Standards*, 49 C.F.R § 193.2057, 2016.

30. Magnussen, B.F. and Hjertager, B.H. *On mathematical modeling of turbulent combustion with special emphasis on soot formation and combustion*. in *Symposium (International) on Combustion*. 1977: Elsevier.

31. Malalasekera, W., Versteeg, H.K., and Gilchrist, K., *A review of research and an experimental study on the pulsation of buoyant diffusion flames and pool fires,* Fire and materials, 1996, **20**(6): p. 261-271.

32. Malvos, H. and Raj, P. *Details of 35 m diameter LNG fire tests conducted in Montoir, France in 1987, and analysis of fire spectral and other data*. in *AIChE Winter Conference, Orlando, FL*. 2006.

33. Mannan, M.S., *LNG Pool Fire Modeling White Paper,* 2008, Mary Kay O'Connor Process Safety Center.

34. McCaffrey, B., *Momentum implications for buoyant diffusion flames,* Combustion and Flame, 1983, **52**: p. 149-167.

35. McGrattan, K., et al., *Fire dynamics simulator, technical reference guide, volume 3: Validation,* NIST Special Publication, 2013, **1018**: p. 3.

36. McGrattan, K., et al., *Fire Dynamics Simulator Technical Reference Guide Volume 1: Mathematical Model,* NIST special publication, 2013, **1018**.

37. McGrattan, K., Rehm, R., and Baum, H., *Fire-driven flows in enclosures,* Journal of Computational Physics, 1994, **110**(2): p. 285-291.

38. McGrattan, K.B., Baum, H.R., and Rehm, R.G., *Numerical simulation of smoke plumes from large oil fires,* Atmospheric Environment, 1996, **30**(24): p. 4125-4136.

39. McGrattan, K.B. and Forney, G.P., *Fire Dynamics Simulator: User's Manual*, 2000: US Department of Commerce, Technology Administration, National Institute of Standards and Technology.

40. McGrattan, K.B., Hostikka, S., and Floyd, J.E., *Fire dynamics simulator, user's guide,* NIST special publication, 2010, **1019**.

41. Melhem, G., Saraf, S., and Ozog, H., *LNG Properties and Hazards, Understand LNG Rapid Phase Transitions (RPT). ioMosaic Corporation, Report no,* An ioMosaic Corporation Whitepaper, 2006: p. 38.

42. Moorhouse, J. *Scaling criteria for pool fires derived from large-scale experiments*. in *The Assessment of Major Hazards, Symposium Series*. 1982.

43. Nedelka, D., Moorhouse, J., and Tucker, R., *The Montoir 35m diameter LNG pool fire experiments,* 1989: Midlands Research Station.

44. Notarianni, K., et al. *Smoke production from large oil pool fires*. in *Interflam*. 1993.

45. Pope, S.B., *Turbulent flows,* 2001: IOP Publishing.

46. Raj, P.K., *Large hydrocarbon fuel pool fires: physical characteristics and thermal emission variations with height.,* Journal of hazardous materials, 2007, **140**(1-2): p. 280-92.

47. Raj, P.K., *Large LNG Fire Thermal Radiation – Modeling Issues & Hazard Criteria Revisited,* Process Safety Progress, 2005, **24**.

48. Raj, P.K., *LNG fires: A review of experimental results, models and hazard prediction challenges,* Journal of hazardous materials, 2007, **140**(3): p. 444-464.

49. Rehm, R.G. and Baum, H.R., *The Equations of Motion for Thermally Driven, Buoyant Flows,* Journal of Research of the National Bureau of Standards, 1978, **83-3**.

50. Rew, P.J. and Hulbert, W.G., *Development of Pool Fire Thermal Radiation Model,* 1996, HSE Contract Research Report.

51. Ris, D., *Modeling techniques for prediction of fires,* Polymeric materials for unusual service conditions, 1973: p. 185-193.

52. Schälike, S., Wehrstedt, K.-D., and Schönbucher, A. *CFD simulation to predict the thermal radiation of large LNG pool fires*. in *Proceedings of the European combustion meeting*. 2011.

53. Thomas, P. *The size of flames from natural fires*. in *Symposium (International) on Combustion*. 1963: Elsevier.

54. Tieszen, S., et al., *Experimental study of the flow field in and around a one meter diameter methane fire,* Combustion and Flame, 2002, **129**(4): p. 378-391.

55. Trouvé, A., *CFD Modeling of Large-Scale Pool Fires,* Fire Safety Science, 2008, **9**.

56. Vembe, B.E., et al., *Kameleon FireEx KFX User manual*, 2010: ComputIT.

57. Versteeg, H.K. and Malalasekera, W., *An introduction to computational fluid dynamics: the finite volume method*, 2007: Pearson Education.

58. Welker, J. and Sliepcevich, C., *Bending of wind-blown flames from liquid pools,* Fire Technology, 1966, **2**(2): p. 127-135.

59. Woodburn, P. and Britter, R., *CFD simulations of a tunnel fire—Part I,* Fire Safety Journal, 1996, **26**(1): p. 35-62.

60. Woodward, J.L.P., Robin M. , *LNG RISK BASED SAFETY : Modeling and Consequence Analysis*, 2010: John Wiley and Sons.

61. Xin, Y., et al., *Fire dynamics simulations of a one-meter diameter methane fire,* Combustion and Flame, 2008, **153**(4): p. 499-509.

62. Xin, Y., et al., *Fire dynamics simulation of a turbulent buoyant flame using a mixture-fraction-based combustion model,* Combustion and Flame, 2005, **141**(4): p. 329-335.

63. Zukoski, E.E., Cetegen, B.M., and Kubota, T., *Visible structure of buoyant diffusion flames,* Symposium (International) on Combustion, 1985, **20**(1): p. 361-366.

APPENDIX

This appendix shows equations for transmissivity and view factor used for the Solid Flame Model.

A. Transmissivity

LNGFIREIII neglects the absorption due to carbon dioxide.

$$\tau = 1 - \alpha_w \qquad \textbf{(A . 1)}$$

$$\alpha_w = \varepsilon_w \left(\frac{T_a}{T_{flame}}\right)^{0.45} \qquad \textbf{(A . 2)}$$

when 0 atm.m <$P_{vL} \leq$0.00005 atm.m,

$$\varepsilon_w = 0$$

when 0.00005 atm.m <$P_{vL} \leq$10 atm.m,

$$\varepsilon_w = 10^{-0.4685+0.34729P_{log}-0.0864P_{log}^2} . e^{\frac{\ln\left(0.72+0.16\,P_{log}\right)\ln\left(\frac{T_a}{500R}\right)}{\ln(3)}}$$

when 10 atm.m <$P_{vL} \leq$ 453 atm.m,

$$\varepsilon_w = \left(1.24 - \frac{0.642}{P_{log}}\right) . e^{\frac{\ln\frac{\left(1.24P_{log}-0.72\right)}{\left(1.24P_{log}-0.642\right)}\,\ln\left(\frac{T_a}{500R}\right)}{\ln(3)}}$$

when 453 atm.m <$P_{vL} \leq$ 1000 atm.m,

$$\varepsilon_w = e^{\frac{\ln\left(1.24-\frac{0.72}{P_{log}}\right)\,\ln\left(\frac{T_a}{500R}\right)}{\ln(3)}}$$

when P_{vL}> 1000 atm,

$$\varepsilon_w = 1$$

$$P_{log} = \frac{\ln(P_{v,L})}{2.302} \qquad \textbf{(A.3)}$$

$$P_{v,L} = P_{v,water}.\frac{T_{flame}}{T_a}(X - width) \qquad \textbf{(A.4)}$$

$$P_{v,water} = RH.e^{14.414 - \frac{9590.56}{T_a R}}\ atm \qquad \textbf{(A.5)}$$

where, τ : Transmissivity

α_w : Absorptivity of water vapor

ε_w : Emissivity of water vapor

T_a : Ambient temperature

T_{flame} : Flame temperature (1300K)

$P_{v,L}$: Amount of water vapor along path, *x*

$P_{v,water}$: Saturated water vapor pressure, *atm*

RH : Relative humidity, *%*

B. View factor

View factor is calculated for a cylindrical tilted flame. The tilt angle, θ, is with respect to the vertical and is positive for distance downwind and negative for upwind direction.

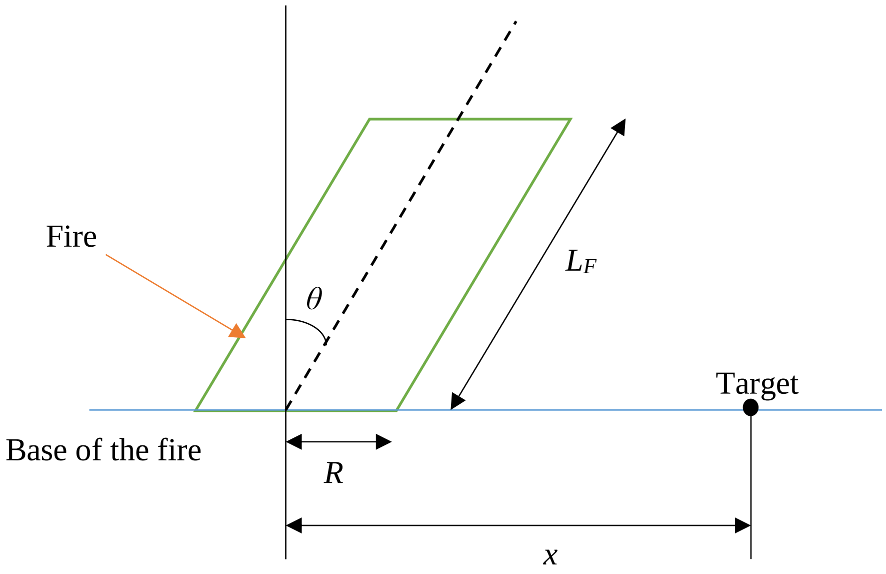

Figure A . 1: Cylindrical flame for view factor calculation.

$$\pi F_v = -E\tan^{-1}D + \frac{E\left(a^2+(b+1)^2-2b(1+a\sin\theta)\right)}{AB}\tan^{-1}\left(\frac{AD}{B}\right) + \frac{\cos\theta}{C}\left[\tan^{-1}\frac{ab-F^2\sin\theta}{FC}+\tan^{-1}\frac{F^2\sin\theta}{FC}\right] \tag{A . 6}$$

$$\pi F_h = \tan^{-1}\left(\frac{1}{D}\right) + \frac{\sin\theta}{C}\left[\tan^{-1}\frac{ab-F^2\sin\theta}{FC}+\tan^{-1}\frac{F^2\sin\theta}{FC}\right] - \frac{E\left(a^2+(b+1)^2-2(b+1+a\sin\theta)\right)}{AB}\tan^{-1}\left(\frac{AD}{B}\right) \tag{A . 7}$$

$$F_{max} = \sqrt{F_v^2 + F_h^2} \qquad \textbf{(A.8)}$$

where,

a = L/R (L_b/R or L_f/R)

b = x/R

$$A = \sqrt{a^2 + (b+1)^2 - 2 \times a \times (b+1) \times \sin\theta}$$

$$B = \sqrt{a^2 + (b-1)^2 - 2 \times a \times (b-1) \times \sin\theta}$$

$$C = \sqrt{1 + (b-1)^2 \times \cos^2\theta}$$

$$D = \sqrt{\frac{b-1}{b+1}}$$

$$E = \frac{a \times \cos\theta}{b - a \times \sin\theta}$$

$$F = \sqrt{(b^2 - 1)}$$